Ultra-Low Dark Current Organic-Inorganic Hybrid X-Ray Detectors

M. Prabodhi A. Nanayakkara, Lidija Matjacic, Sebastian Wood, Filipe Richheimer, Fernando A. Castro, Sandra Jenatsch, Simon Züfle, Rachel Kilbride, Andrew J. Parnell, Mateus G. Masteghin, Hashini M. Thirimanne, Andrew Nisbet, K. D. G. Imalka Jayawardena, S. Ravi P. Silva*

M. P. A. Nanayakkara, M. G. Masteghin, Dr H. M. Thirimanne, Dr K. D. G. I. Jayawardena, Prof. S. R. P. Silva
Advanced Technology Institute, Department of Electrical and Electronic Engineering, University of Surrey, Guildford, Surrey, GU2 7XH, United Kingdom.
E-mail: s.silva@surrey.ac.uk

Dr L. Matjacic, Dr S. Wood, F. Richheimer, Dr F. A. Castro
National Physical Laboratory, Teddington, Middlesex, TW11 0LW, UK.

Dr S. Jenatsch, Dr S. Züfle
FLUXiM AG, Katharina-Sulzer-Platz 2, 8400 Winterthur, Switzerland.

R. Kilbride, Dr A. J. Parnell
Department of Physics and Astronomy, University of Sheffield, Hicks Building, Sheffield, S3 7RH, UK.

Prof. A. Nisbet
Department of Medical Physics and Biomedical Engineering, University College London, Gower St, Bloomsbury, London WC1E 6BT, UK.

Abstract

Organic-inorganic hybrid semiconductors are an emerging class of materials for direct conversion X-ray detection due to attractive characteristics such as high sensitivity and the potential to form conformal detectors. However, existing hybrid semiconductor X-ray detectors display dark currents that are ×1000 - 10000 higher than industrially relevant values of 1-10 pA mm^{-2}. Herein, we report ultra-low dark currents of <10 pA mm^{-2}, under electric fields as high as ~4 V μm^{-1}, for hybrid X-ray detectors consisting of bismuth oxide nanoparticles (for enhanced X-ray attenuation) incorporated into an organic bulk heterojunction consisting of p-type Poly(3-hexylthiophene-2,5-diyl) (P3HT) and n-type [6,6]-Phenyl C71 butyric acid methyl ester (PC$_{70}$BM). Such ultra-low dark currents are realized through the enrichment of the hole selective p-type organic semiconductor near the anode contact. The resulting detectors demonstrate broadband X-ray response including an exceptionally high sensitivity of ~1.5 mC Gy^{-1} cm^{-2} and <6% variation in angular dependence response under 6 MV hard X-rays. The above characteristics in combination with excellent dose linearity, dose rate linearity, and reproducibility over a broad energy range enable these detectors to be developed for medical and industrial applications.

1. Introduction

Optoelectronic devices based on organic semiconductors are gaining significant attention, due to the possibility of fabricating detectors whose response can be tuned over a broad energy range on flexible architectures that can be manufactured using low-cost roll-to-roll and sheet-to-sheet printing techniques.[1] Recently, the use of these devices has been expanded for X-ray detection, with the potential for a wide range of applications including medical diagnostics, industrial inspection, and scientific research (e.g. crystallography). Strategies used for the adoption of organic semiconductors for X-ray detection include the incorporation of high-atomic number (Z) elements into the semiconductor structure[2] and the incorporation of high-Z direct converting nanoparticles (NPs)[3–5] or scintillators[6] into an organic bulk heterojunction (BHJ) matrix. In particular, the direct conversion X-ray detection strategy developed by Thirimanne et al.,[1] where high atomic number bismuth oxide (Bi_2O_3) nanoparticles were incorporated into an organic BHJ consisting of p-type Poly(3-hexylthiophene-2,5-diyl) (P3HT) and n-type [6,6]-Phenyl C71 butyric acid methyl ester ($PC_{70}BM$), demonstrated appealing characteristics such as low voltage operation and high sensitivity over a broad energy range. The concept was further expanded by Jayawardena et al.[7] to demonstrate X-ray imaging.

Despite the promise shown by the above NP incorporated BHJ (NP-BHJ) direct conversion X-ray detectors, they suffer from high dark currents of $\sim 10^4$ pA mm^{-2} under an applied bias of -10 V (equivalent to an electric field of ~ 0.4 V μm^{-1}). This value is well above the dark current values of 10 pA mm^{-2} exhibited by state-of-the-art X-ray detectors.[8] As low dark currents are an important metric that enable the detection of low dose rates and a good dynamic range, it is important to develop routes to minimize dark currents in these hybrid detectors.

One possible reason behind such high dark currents is the poor charge selectivity at the device contacts. The use of poly(3,4-ethylenedioxythiophene): poly(styrene sulfonate) (PEDOT: PSS) as the hole transport layer (HTL) is known to result in poor charge selectivity in organic photovoltaics and photodetectors.[9] In addition, the use of PEDOT: PSS has also been

3

demonstrated to result in the rapid degradation of optoelectronic characteristics of organic devices. This has been identified due to the hygroscopic nature of PEDOT: PSS which results in the corrosion of indium tin oxide (ITO).[10] Such deleterious effects can be minimized through the adoption of the inverted device architecture based on alternate (hole) transport layers. For example, as previously shown by us,[11] photovoltaic devices based on a standard architecture with PEDOT: PSS as an HTL degrade rapidly to 20% of their starting performance within 200 h of storage in air. In comparison, inverted devices with a metal oxide HTL showed a more stable performance degrading to only 80% of their starting performance under the same storage conditions within the same period.

Here, we report a route towards achieving ultra-low dark currents that are below 10 pA mm^{-2}, even under high electric fields of ~4 V µm^{-1} in HTL free, inverted NP-BHJ direct conversion X-ray detectors where Bi_2O_3 NPs are used for enhancing the X-ray attenuation, while P3HT and $PC_{70}BM$ are used for the extraction of the X-ray generated holes and electrons, respectively. Such ultra-low dark currents are achieved as a result of the enrichment of the p-type P3HT semiconductor near the anode contact due to the formation of a vertical composition gradient within the active semiconductor blend, resulting in X-ray detectors with an exceptional performance, even without the addition of an external HTL. To the best of our knowledge, this is the first report, that uses vertical phase segregation in BHJ blends to achieve highly efficient charge blocking which results in the lowest dark currents reported so far for organic or hybrid X-ray detectors (**Figure 1**a). The resulting detectors demonstrate broadband response with sensitivities of ~60 nC Gy^{-1} cm^{-2} under 70 kV X-ray irradiation and a remarkably high sensitivity of around ~1.5 mC Gy^{-1} cm^{-2} under 6 MV photon irradiation from a medical linear accelerator. Furthermore, these NP-BHJ detectors with low dark currents demonstrate excellent dose linearity and dose rate linearity, reproducibility, and low beam incidence angle dependence. Such features enable these detectors to be well suited commercially for imaging and dosimetry in medical and industrial applications.
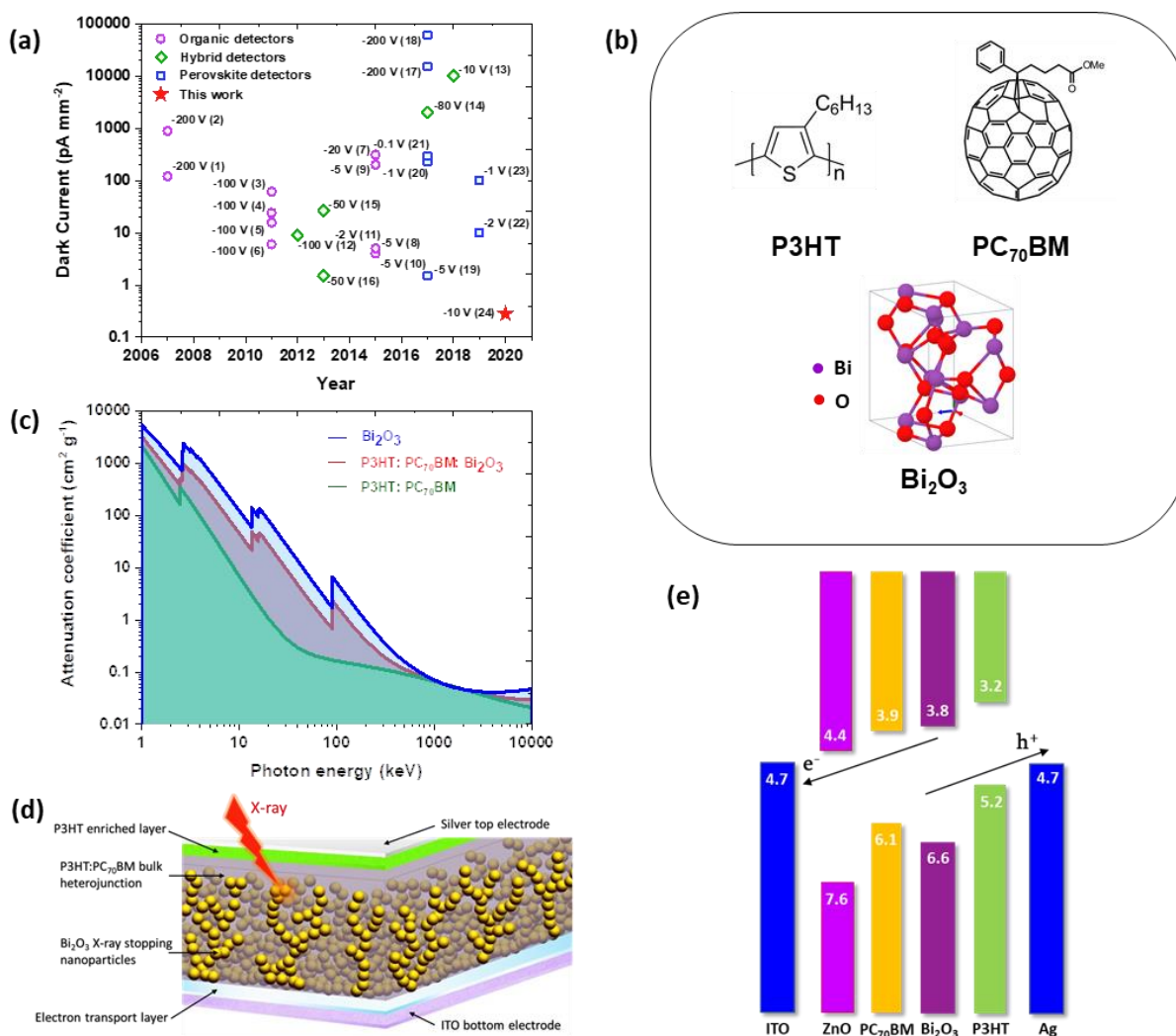
4

Figure 1. Organic-inorganic hybrid X-ray detectors enabling ultra-low dark currents. (a) Comparison of the dark current response characteristics of the recently developed organic and organic-inorganic hybrid direct conversion X-ray detectors. (1)-(2),[12] (3)-(6),[13] (7),[14] (8)-(10),[15] and (11)[16] are organic X-ray detectors, (12),[3] (13),[1] (14),[5] (15)-(16),[4] are organic-inorganic hybrid X-ray detectors fabricated by incorporating high-Z NPs, (17),[17] (18),[18] (19),[19] (20)-(21),[20] (22),[21] and (23)[22] are perovskite based X-ray detectors ,and (24) is the X-ray detector developed in this work. The operating voltage is given adjacent to each data point. (b) Chemical structure of P3HT, PC$_{70}$BM, and Bi$_2$O$_3$. (c) Comparison of the mass attenuation coefficient of Bi$_2$O$_3$ NPs, organic BHJ consisting of P3HT and PC$_{70}$BM, and the P3HT: Bi$_2$O$_3$: PC$_{70}$BM blend indicating the enhancement of X-ray attenuation by incorporation of high-Z NPs. (d) Schematic of the NP-BHJ X-ray detector architecture used in this work. (e) Flat band diagram for the device architecture used in this work. All energy values are given in eV.

2. Results and Discussion

2.1. Response Characteristics of the NP-BHJ X-Ray Detectors

The organic-inorganic hybrid X-ray absorber used herein consists of high-Z direct converting

Bi$_2$O$_3$ NPs (average particle size of 38 nm) as the X-ray absorber, while the P3HT and PC$_{70}$BM

form percolation pathways for extraction of holes and electrons (respectively) (Figure 1b, c). For this study the P3HT: $PC_{70}BM$ weight ratio was fixed at 1:1. While lowering $PC_{70}BM$ fraction relative to P3HT has been demonstrated to result in trap-assisted gains in photoconductivity,[23] this mechanism can also degrade the response time of the detectors as has been shown by Basiricò et al.[24] Furthermore, for this study, the P3HT: $PC_{70}BM$: Bi_2O_3 weight ratio was fixed at 1:1:1. However, we note that increasing the Bi_2O_3 weight fraction allows further improvements in detector sensitivity due to the resulting increase in X-ray attenuation.[1] The X-ray detectors were fabricated in an inverted device architecture where the NP-BHJ composite was sandwiched between ITO and silver (Ag) electrodes (Figure 1d) resulting in a glass/ITO/zinc oxide/NP-BHJ/HTL/Ag architecture, enabling both electron and hole extraction (Figure 1e). Using thermogravimetric analysis (TGA), the NP loading in the film (by weight) was estimated to be 38.1% (Figure S1, Supporting Information) which is slightly higher than the NP loading in the starting ink (33.3 %). This is attributed to the use of non-functionalized NPs which can lead to some variation in the NP distribution within the ink. Initially, we studied the influence of varying the NiO HTL thickness, on both the dark current and the X-ray photocurrent response (under 70 kV X-ray radiation) for a NP-BHJ film thickness of 55 µm. The NiO HTL thickness was altered by changing the NiO NP concentration in the starting ink from 2.5, 1.25, 0.63, 0.31 to 0.16 wt. %. As observed from **Figure 2**a, reducing the NiO HTL thickness has little influence on the dark current densities of these detectors which are measured to be less than 0.5 pA mm^{-2} (at an applied bias of -10 V). This is more than an order of magnitude lower than the industrially accepted dark current density of 10 pA mm^{-2}.[8] The lack of sensitivity of the detector dark current to the NiO HTL thickness, coincides with the lack of variation of the surface roughness of the NiO HTLs with NiO HTL thickness, thereby indicating no Fowler-Nordheim tunneling induced dark current enhancements[25] (Figure S2 and Table S1, Supporting Information). Further, we did not observe a noticeable variation in the X-ray sensitivity of these detectors irrespective of the NiO HTL thickness used (The X-ray

response characteristics of the NiO-based detectors are given in Note S1, Figure S3, and Figure S4, Supporting Information). In comparison to the above, devices fabricated without an HTL (HTL Free detectors, HTLFDs) showed a similar X-ray sensitivity with an even lower dark current response of 0.28 pA mm^{-2} at -10 V (Figure 2a). The slightly higher dark current response observed for NiO-based detectors compared to HTLFDs is attributed to the presence of unintentional dopants incorporated through starting chemicals used for the synthesis of such NPs, and the defect states due to missing lattice sites (e.g. oxygen vacancies) in such metal oxide systems.
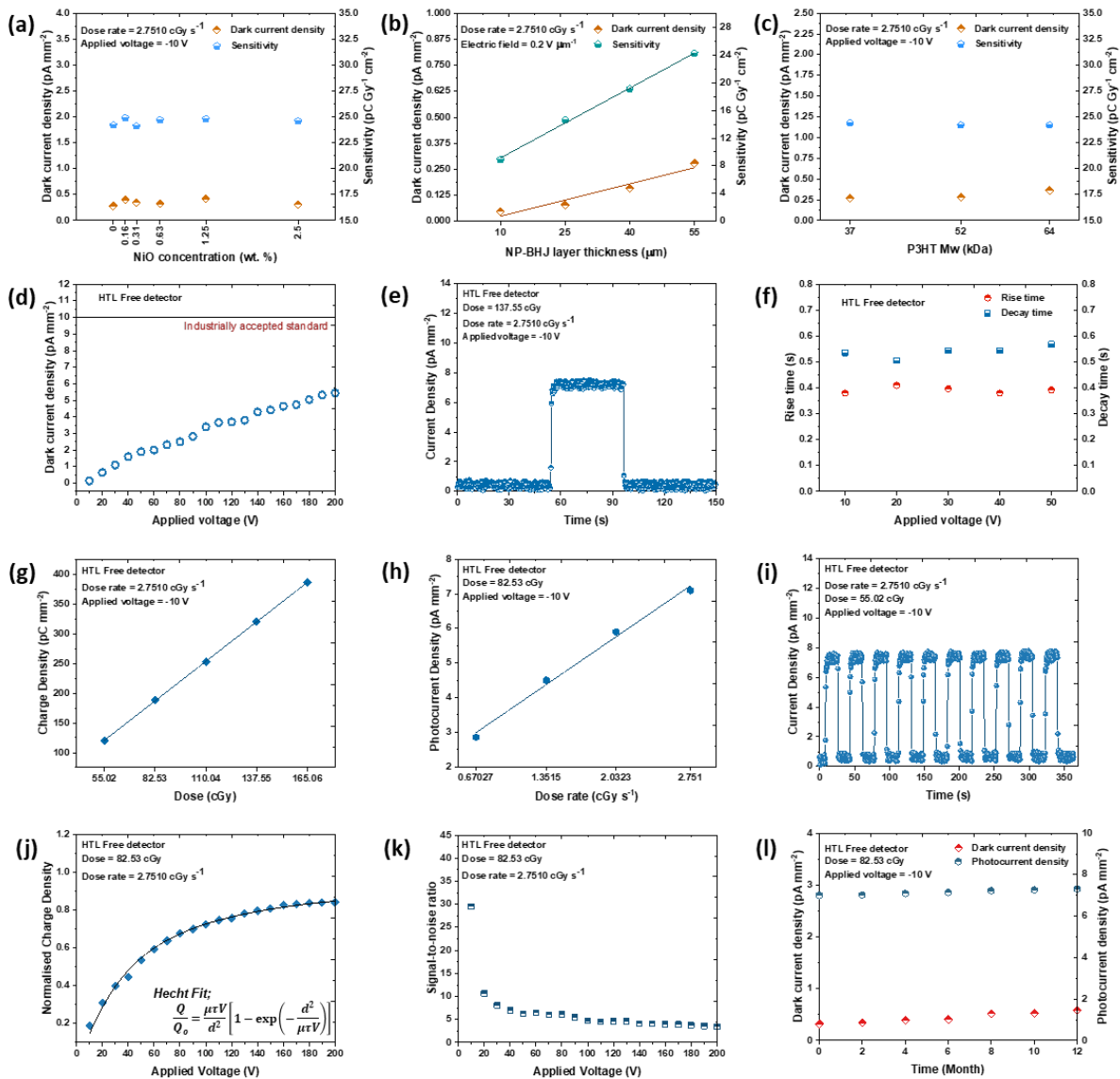

Figure 2. Response characteristics of the NP-BHJ detectors under 70 kV X-rays. (a) Dark current and sensitivity as a function of NiO concentration. (b) Dark current and sensitivity of the HTLFD as a function of NP-BHJ layer thickness. (c) Dark current and sensitivity of the

HTLFD as a function of P3HT *Mw*. (d) Dark current density as a function of applied bias of the HTLFD. (e) Transient X-ray photocurrent response from the HTLFD indicating a "square shaped" response. (f) Rise time and decay time of the detector as a function of applied bias. (g) Dose and, (h) Dose rate dependence for the HTLFD. The solid lines indicate linear fits. Both the dose as well as dose rate dependence shows excellent linearity ($R^2 > 0.9998$). (i) Reproducibility of the X-ray photocurrent response of the HTLFD under repeated X-ray exposures. (j) Voltage dependence of the detector together with the Hecht fit ($R^2 > 0.9998$) for estimation of the μτ product. (k) SNR variation with applied bias. A drop in SNR is observed due to increase in the dark current and saturation of the X-ray photocurrent with increasing voltage. (l) Overtime stability of the dark current and photocurrent response of the detector.

Following the above, we proceeded to investigate the influence of the NP-BHJ layer thickness, as well as the molecular weight (*Mw*) of P3HT on the dark current response and X-ray sensitivity of the HTLFDs. To study the influence of the thickness, we varied the thickness of the NP-BHJ layer over the range of 10 - 55 μm. For this study, the detector dark currents and X-ray sensitivities were compared for measurements done under a similar electric field. Here, the sensitivity (*S*) of an X-ray detector[6] is defined as:

$$S = \frac{Q}{DA} = \frac{\int (I_{X-ray}(t) - I_{Dark})dt}{DA} \tag{1}$$

where, Q represents the charge generated under irradiation, I_{X-ray} and I_{Dark} represent the current under X-ray irradiation and in the dark, respectively, D is the X-ray incident dose, and A is the active area of the detector. The sensitivity was estimated based on the slope of the charge density vs. dose curve.

Both the dark current density as well as the X-ray sensitivity showed an approximately linear increase with increasing thickness (Figure 2b). The increase in sensitivity with increasing NP-BHJ thickness is in agreement with the increased X-ray absorption as a result of increasing the film thickness. The linear increase in dark current density with thickness indicates that the conductivity also increases with the thickness of the NP-BHJ layer. Recently, it has been demonstrated that organic photodiodes can be highly sensitive to low light, more so than conventional silicon photodiodes.[26] While a light-tight box has been employed in our study to minimize the impact of stray light, the ultra-low dark currents achieved in this work is likely to

enhance the sensitivity of these NP-BHJ detectors to exceptionally low light conditions. This also points the need towards integrating appropriate stray light blocking strategies such as the use of Vantablack® coatings,[27] especially when applying these detectors to measure exceptionally low X-ray dose rates. However, despite such effects we note that ultra-low dark currents of less than 0.3 pA mm^{-2} are still maintained irrespective of the thickness, suggesting that the underlying mechanism for the charge blocking nature at the contacts remains unchanged, irrespective of the thickness variation. To study the influence of the P3HT Mw on the detector characteristics, we evaluated the performance of HTLFDS fabricated using P3HT with Mws of 37, 52 and 64 kDa for a constant NP-BHJ thickness of 55 µm. We again observed an insensitivity of the dark current as well as the X-ray sensitivity of the HTLFDs to the P3HT Mw (Figure 2c). This indicates that the charge blocking mechanism is also independent of the Mw of the material used.

We now proceed to discuss in detail, the X-ray photocurrent response characteristics of the above HTLFDs with a NP-BHJ layer thickness of 55 µm. The results presented are for a P3HT Mw of 52 kDa, as similar characteristics were observed for the other P3HT Mws studied in this work. We initially studied the influence of increasing the applied (reverse) bias from -10 V to -200 V (i.e., equivalent to macroscopic electric fields in the range of ~0.2 V µm^{-1} to ~4 V µm^{-1}) on dark current response. The possibility to operate under high electric fields is desirable in order to extract charges generated throughout the thickness of the NP-BHJ film. Despite the relatively high electric fields used, the dark current densities were below 6 pA mm^{-2}, even under an electric field of ~4 V µm^{-1} (Figure 2d) which is still lower than the industrial requirement of 10 pA mm^{-2}. The HTLFDs also displayed a "square shaped" X-ray photocurrent response with a sharp rise and decay (Figure 2e) when exposed to X-rays from the 70 kV source. This is contrary to the saw-tooth shaped transient photocurrent response reported for a number of organic semiconductor-based X-ray detectors[7,24] or for NP-BHJ detectors that used PEDOT: PSS as the HTL in combination with a conventional device architecture.[1] The observation of

saw-tooth shaped characteristics has been attributed to the photoconductive gain mechanisms in mono-carrier type devices.[24] The lack of such a characteristic in the devices studied here suggests a more balanced, X-ray generated electron and hole extraction mechanism to be prevalent in these devices. Using the X-ray photocurrent response characteristics obtained, we evaluated the response speed of the NP-BHJ detector based on the rise time (time to achieve 63% of the saturated X-ray photocurrent signal) and decay time (time to achieve a current density that is 37% of the saturated X-ray photocurrent signal) as a function of applied bias. Both the rise and decay times were estimated to be ~0.3 s and ~0.5 s (respectively) regardless of the applied bias (Figure 2f). However, the accuracy of these values is limited by the settling time of the X-ray source used. We anticipate the actual detector rise and decay times to be in the 10 - 100 µs time scale (as observed when characterized under visible light as discussed later). Furthermore, these time constants are a significant improvement over those observed for NP-BHJ detectors that utilize PEDOT: PSS as an HTL where rise and decay times over several seconds were observed.[1] The improvements in rise and decay times achieved here are beneficial in mitigating ghosting induced artefacts in imaging and dosimetry. We also evaluated linearity of the X-ray generated charge under varying X-ray dose (Figure 2g) and the linearity of the X-ray photocurrent response under varying dose rate (Figure 2h). In both cases, an excellent linear behavior was observed with $R^2 > 0.9998$. Based on the dose linearity studies, we estimated the sensitivity of HTLFDs to be ~24.2 nC Gy^{-1} cm^{-2} (at -10 V) and ~61 nC Gy^{-1} cm^{-2} (at -200 V). We further studied the reproducibility of the detector response characteristics through exposure to ten consecutive X-ray pulses (Figure 2i). The reproducibility of the X-ray response of the detector was quantitatively assessed by normalizing the charge extracted under each exposure to that of the initial exposure. This analysis indicated the maximum deviation of the detector response was less than 2.3 %, indicating a very good reproducibility due to minimal charge trapping effects. The mobility-lifetime ($\mu\tau$) product is a key metric used in comparing the charge transport properties in semiconductors used for X-ray detection. The relationship

between the $\mu\tau$ product, applied voltage, and the collected charge is described by the Hecht equation[7] given below:

$$Q = Q_o \frac{\mu\tau V}{d^2}\left[1 - exp\left(-\frac{d^2}{\mu\tau V}\right)\right]$$ (2)

where, Q is the total charge extracted, Q_o the asymptotic charge, V the applied voltage, d the detector thickness, μ the charge carrier mobility, and τ the charge carrier lifetime. To evaluate the $\mu\tau$ product for the NP-BHJ detectors, the voltage dependence of the X-ray photocurrent response of the detector was studied from -10 V to -200 V under a constant dose and dose rate. The curve was fitted with the Hecht relationship (Figure 2j) which showed that the $\mu\tau$ product of the detector is ~10^{-7} cm^2 V^{-1}. This result is within 1-2 orders of magnitude of the values reported for thick NP-BHJ X-ray photoconductors (~1.7×10^{-6} cm^2 V^{-1})[7] and stabilized a-Se photoconductors (2×10^{-6} to 2×10^{-5} cm^2 V^{-1}).[28] The signal to noise ratio (SNR) (evaluated as the ratio between the photocurrent density and dark current density) of the detector was evaluated as a function of applied voltage as shown in Figure 2k. The SNR displayed a decaying characteristic due to the increase in dark current with voltage (discussed previously) as opposed to the Hecht-type relationship observed for the X-ray photocurrent which saturates at high voltages. The high SNR at low operating voltages indicates the potential of these detectors for low power sensing applications, such as wearable dosimeters. We also evaluated the stability of the detector characteristics by measuring the dark current and X-ray photocurrent response of a detector (stored in a N$_2$ environment in between measurements) over a 12-month time period (Figure 2l). Although an increase in the dark current density was observed, the dark currents were still less than 1 pA mm^{-2} (at -10 V), well within industrially accepted values. In comparison, the X-ray photocurrent response did not show a noticeable increase. The good stability observed for both dark current and X-ray photocurrent indicates the excellent structural stability of the NP-BHJ system.

2.2. Formation of a Charge Selective Layer within the NP-BHJ Film

Based on the detector response characteristics observed under 70 kV soft X-ray radiation, it is evident that the HTLFDs have ultra-low dark currents (i.e., sub 0.3 pA mm^{-2} at -10 V) and a similar X-ray sensitivity to detectors with an HTL. This indicates the formation of an internal hole selective/electron blocking layer closer to the anode. As noted previously, in the NP-BHJ detector concept, the two organic semiconductors P3HT and PC$_{70}$BM are used to achieve efficient transport of holes and electrons (respectively) generated within the Bi$_2$O$_3$ NPs upon X-ray attenuation. The efficient extraction of charge is expected to be enabled through the formation of a three-dimensional bi-continuous percolating network, similar to that found within organic photovoltaics. However, it is possible that the NP-BHJ film formation process may have resulted in a phase-separation process, leading to the enrichment of the p-type P3HT closer to the anode contact, thereby resulting in ultra-low dark currents irrespective of the thickness of the NP-BHJ layer as well as the *Mw* of P3HT used.

In order to identify the nature of the electronic contact formed between the NP-BHJ surface and the silver anode, we carried out scanning Kelvin probe microscopy (SKPM) measurements, which (**Figure 3**a) indicate the average surface potential of the hybrid layer to be approximately 4.6 eV. The near similarity of this surface potential to the work function of silver (4.7 eV)[29] is likely to facilitate the formation of an ohmic contact between the silver anode and the hybrid layer. To understand the compositional gradient within the NP-BHJ film, we then carried out cross-sectional analysis (Figure 3b). Based on the detection of backscattered electrons in a scanning electron microscope, we observed the enrichment of Bi$_2$O$_3$ NPs (observed as bright regions in the image) at the bottom of the hybrid film (i.e., closer to the electron transport layer), resulting in an organic semiconductor rich capping layer. To identify the vertical chemical compositional profile of the NP-BHJ film and the composition of this capping layer, we carried out time-of-flight secondary ion mass spectrometry (ToF-SIMS) depth profiling (Figure 3c). In order to obtain more information from the organic material, an Ar-GCIB source with

$Ar^+_{1700-2000}$ ion beam was used in this study which introduces less damage when compared to the monoatomic ion beams.[30] Figure 3d illustrates the 3D renderings which describe the distribution of the negative ion species of interest across the film (X=Y=50 μm, Z~55 μm). It can be seen that the S^- (Sulphur) signal, due to the presence of P3HT is the strongest, and uniform throughout the thickness, whereas the C^-_{70} signal due to PC$_{70}$BM and the $Bi_2O^-_3$ signal due to Bi$_2$O$_3$ NPs is confined to the bottom of the film (where the latter is in agreement with the observations made through cross-sectional imaging as discussed above). This confirms our hypothesis on the enrichment of the p-type P3HT near the top surface (Figure 3e), which acts as an efficient electron blocking/hole selective layer within the device architecture studied here.
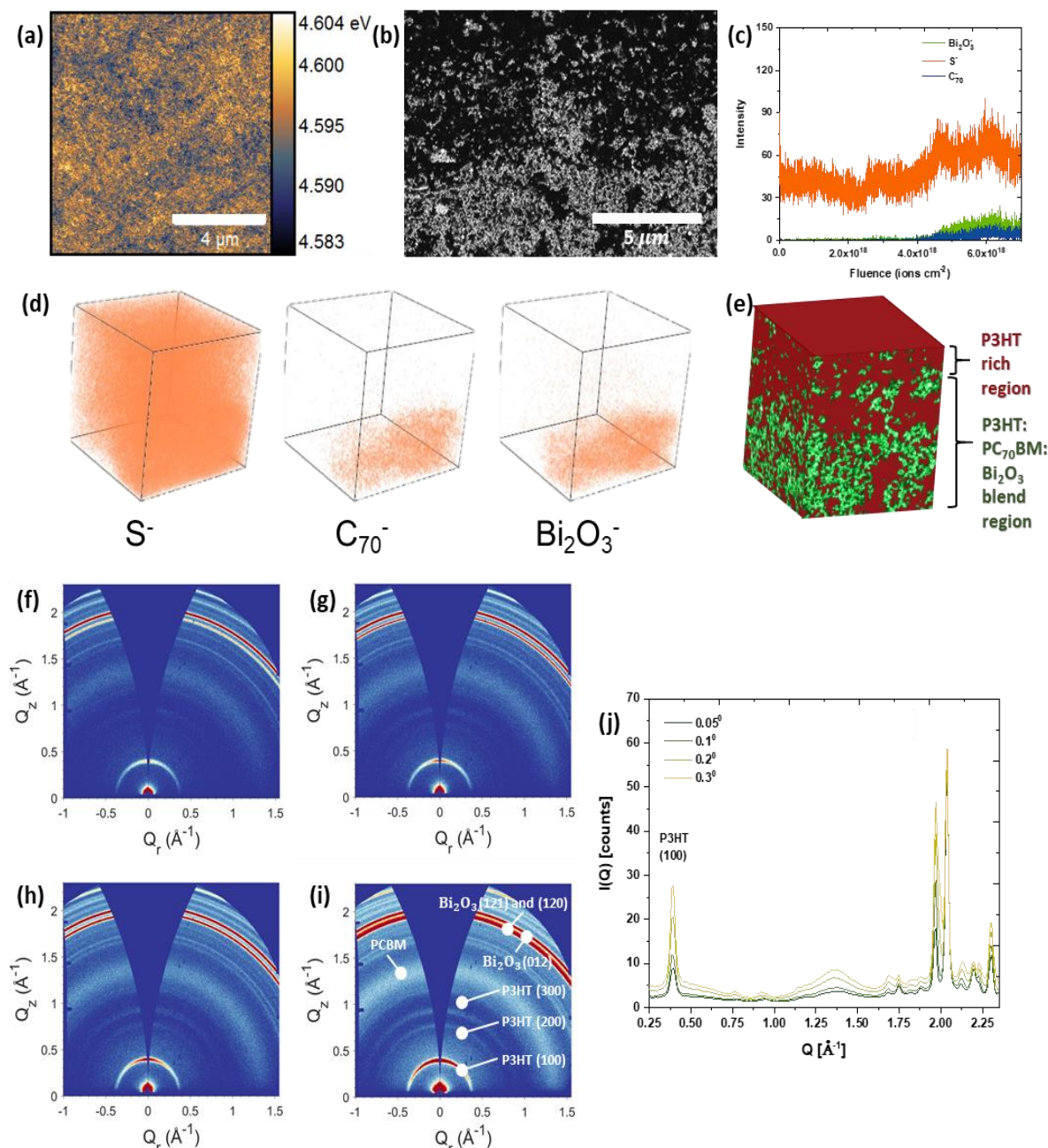
Figure 3. Formation of a p-type charge selective layer within the NP-BHJ film. (a) SKPM micrograph of the NP-BHJ film indicating an average surface potential of ~4.6 V. (b) Cross-sectional micrograph of the NP-BHJ film depicting the accumulation of Bi_2O_3 NPs at the bottom of the film. The bright clusters represent the Bi_2O_3 NP aggregates while the dark regions represent the organic content. (c) Depth profile of the NP-BHJ film obtained from ToF-SIMS depicting the distribution of ion species S^-, C_{70}^-, and $Bi_2O_3^-$ along the film depth. (d) 3D renderings of the negative polarity data (X=Y=50 μm, Z~55 μm) obtained from ToF-SIMS for the S^-, C_{70}^-, and $Bi_2O_3^-$ ions showing the P3HT enrichment at the top surface. (e) Schematic of the NP-BHJ film illustrating the vertical composition gradient resulting in a P3HT rich top region and an organic–inorganic mixed bottom region. 2D GIWAXS spectra for the NP-BHJ film obtained at (f) 0.05°, (g) 0.1°, (h) 0.2°, and (i) 0.3° incident angles indicating the increase of the (100) peak signal at $Q_z \simeq 0.4 \, \overset{o}{A}^{-1}$ with depth. (j) 1D radial integrations of the NP-BHJ film for various incidence angles. A decrease in the (100) P3HT peak width with increasing incidence angle is observed.

14

To understand the nature of crystallinity of the P3HT enriched phase, we conducted grazing incidence wide-angle X-ray scattering (GIWAXS) on the NP-BHJ films. Below the critical angle ($\alpha_c \approx 0.12°$), X-rays travel as an evanescent plane wave along the sample surface probing the near surface features of the film (the top ~10 nm) whereas angles above the critical angle give information about the bulk of the film.[31] GIWAXS spectra were acquired at incident angles 0.05° and 0.1°($\alpha_i < \alpha_c$), as well as 0.2° and 0.3° ($\alpha_i > \alpha_c$) to enable probing of the sub-surface as well as the "bulk" region (up to ~2μm depth) (Figure 3f-i). We noticed the presence of a narrow peak at $Q_z \simeq 0.4 \overset{o}{A}^{-1}$ corresponding to the (100) lamellar stacking of P3HT polymeric chains,[32] indicating the crystallization of the P3HT phase across the examined film depth. Furthermore, based on the higher intensity of the P3HT (100) peak along the Q_z axis, it is evident that the P3HT crystallites formed in the NP-BHJ film have predominantly adopted edge-on orientation where π-π stacking is in the plane of the film and alkyl side chains are perpendicular to the substrate.[31] The average P3HT crystallite size was calculated using the Scherrer formula[31] (equation (3)) on the P3HT (100) peak in the 1D radial integration plots (Figure 3j):

$$D = \frac{K\lambda}{\beta\cos(\theta)} \tag{3}$$

Here, D is the crystallite size, K is the dimensionless shape factor (0.94), λ is the X-ray wavelength (0.134 nm), β is the full width at half maximum (FWHM) of the P3HT (100) peak in radians, and θ is the Bragg angle in radians. The FWHM was estimated by Gaussian fitting of the P3HT (100) peak for each incident angle. An increase in the P3HT crystallite size was observed with the incident angle suggesting that the degree of crystallinity of the P3HT phase is increasing as one moves away from the film surface towards the bulk (Table S2, Supporting Information).

2.3. Physical Mechanism Underlying the Formation of a Charge Selective Layer

The phase segregation behavior in BHJ systems such as those observed in this work can be explained based on the Flory-Huggins theory where the interaction parameter, χ is used to describe the compatibility between two components.[33] A low value for χ allows more homogenous vertical profile to be achieved, while a high value for χ results in a higher degree of phase separation. The χ value of a material blend is related to the surface free energies (γ) of the components in the blend where a higher difference between the γ of the components results in a higher value for χ, thus leading to a larger degree of phase separation. Furthermore, in the instance of film formation, the component(s) with the lowest γ will tend to segregate at the film surface in order to minimize the surface free energy of the final film.

In order to verify whether the phase segregation mechanism described above can take place in the blends studied in this work, we estimated γ of the P3HT films with different Mw s, and of the $PC_{70}BM$ film. We estimated a γ of ~22 N m^{-1} for P3HT irrespective of the Mw. Furthermore, this was also noticeably lower compared to the γ of $PC_{70}BM$ film (~32 N m^{-1}). This significant difference in γ of the organic semiconductors not only drives the phase separation behavior but also the lower γ for P3HT results in the segregation of this semiconductor material at the film surface as explained above. This mechanism therefore clarifies the observation of lower $PC_{70}BM$ content closer to the film surface in ToF-SIMS analysis, which is also indirectly verified through γ values of ~22 N m^{-1} estimated for the NP-BHJ films. Furthermore, the Flory-Huggins theory also helps to explain the low dark currents observed for HTLFDs despite thickness variation, as well as the insensitivity of detector dark currents despite varying the Mw of P3HT. In addition, this allows the design of appropriate detector architectures (either inverted or regular), and identify the need for (or lack of) additional charge selective layers for emerging organic semiconductor systems through the surface free energy measurements for each component in the blend, enabling rapid screening and development to be performed.

2.4. Charge Transport and Extraction Mechanism for Ultra-Low Dark Currents

Based on the insight obtained from the above measurements, the X-ray generation of charges, their transport through the NP-BHJ film and extraction can be explained as outlined in **Figure 4** (the schematics are based on the formation of a P3HT rich surface layer as observed in this study). Within the NP-BHJ ternary system, the Bi_2O_3 NPs attenuate the incident X-rays resulting in the generation of free electrons and holes. The alignment of the Highest (Lowest) Occupied Molecular Orbital of the p-type P3HT (n-type $PC_{70}BM$) with the Valence (Conduction) Band of Bi_2O_3 is such that, it allows the transfer of holes (electrons) to P3HT ($PC_{70}BM$) (Figure 4a). The transfer of electrons (holes) from Bi_2O_3 to P3HT ($PC_{70}BM$) is prevented due to the energy barrier formed as a result of the band alignment as shown in Figure 4a. The holes and electrons are then transported through P3HT and $PC_{70}BM$ (respectively). At the cathode contact, the use of the ZnO as the electron transport layer allows the extraction of electrons from $PC_{70}BM$ while the shallow work function of ZnO prevents the transfer of holes from P3HT to ZnO, thereby minimizing electron-hole recombination at this contact (Figure 4b, c). At the anode contact, the holes transported through the P3HT phase are transferred to the NiO layer from the P3HT rich surface layer (for devices containing a NiO HTL) and extracted through the Ag contact (Figure 4b) or, are transferred directly from P3HT rich surface layer to the Ag contact for the HTLFDs (Figure 4c). In the latter scenario, the P3HT rich surface layer also act as an electron blocking layer which prevents the transfer of electrons from the $PC_{70}BM$ phase to the Ag contact. This electron blocking nature of P3HT in combination with the formation of an ohmic contact between P3HT and silver (as explained based on Figure 3a) enables the fabrication of HTL Free X-ray detectors with dark currents that are similar or lower than those devices incorporating NiO as an HTL while maintaining a similar detector sensitivity.
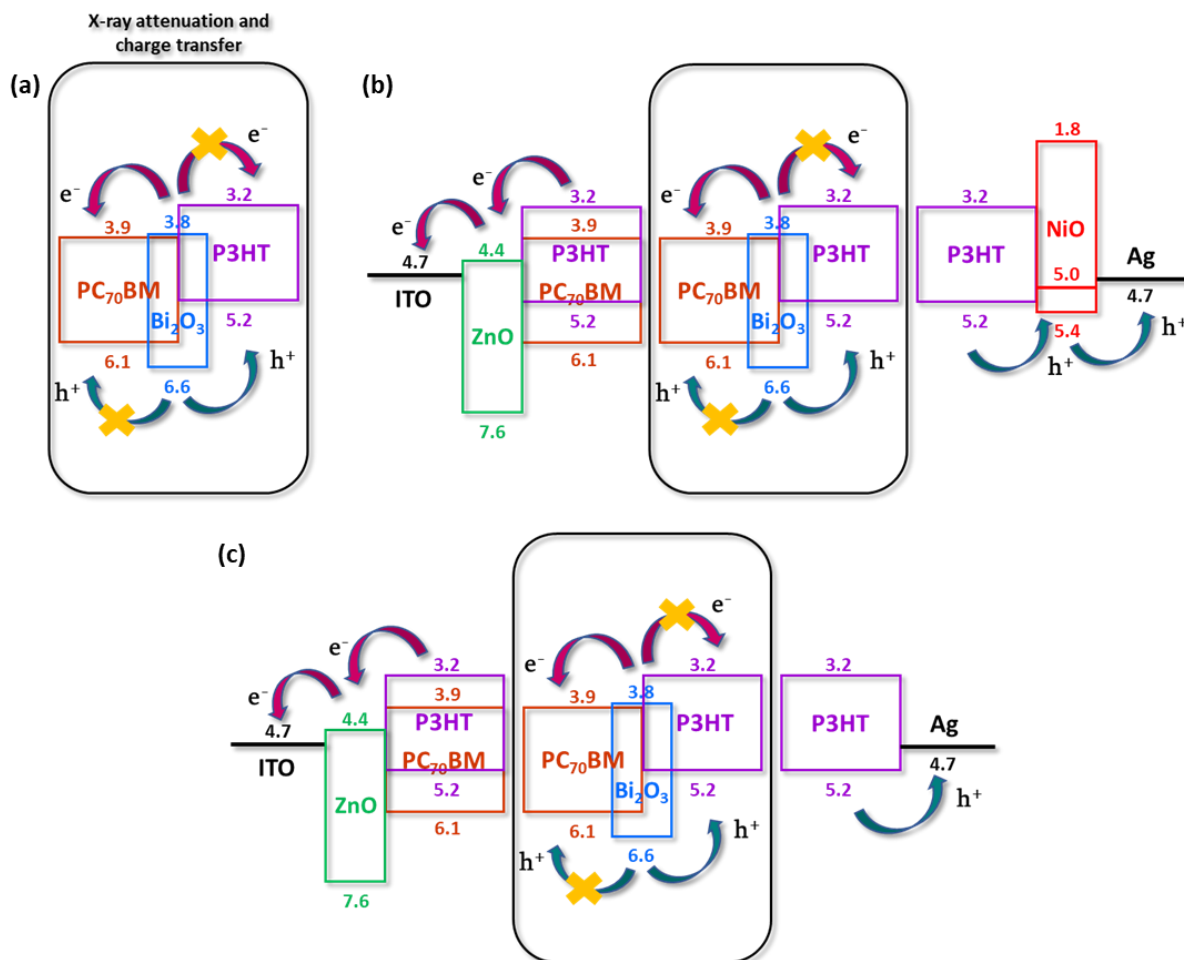
Figure 4. Charge generation, transport, and extraction mechanism in NP-BHJ detectors. (a) The X-rays absorbed by Bi_2O_3 results in the generation of free electrons and holes which are transferred to $PC_{70}BM$ and P3HT (respectively) and transported through these phases. Closer to the anode contact where a P3HT rich region is formed, the holes are either (b) directly injected to the NiO HTL and extracted through the Ag anode or (c) directly injected from the P3HT rich region to the Ag anode. The formation of a P3HT rich region at the film surface minimizes any direct contact between the Ag contact and $PC_{70}BM$. In both (b) and (c), the presence of a BHJ closer to the cathode can result in recombination at the cathode contact. This is mitigated by the electron selective ZnO layer which blocks the transfer of holes from P3HT while allowing the transfer of electrons from $PC_{70}BM$ to ITO.

2.5. Charge Transport Characteristics of the NP-BHJ X-Ray Detectors

Following the identification of the vertical phase segregation that takes place within the NP-BHJ layer, we proceeded to study the charge transport properties of the system that was facilitated by the organic semiconductors used. The charge carrier mobility of the NP-BHJ detectors was estimated using the "photo-charge carrier extraction by linearly increasing voltage" (photo-CELIV) method. We note that the broadband nature of the illumination source

which extends up to ~700 nm enables generation of excitons at the absorption edge of P3HT. Since P3HT has a very low optical absorption coefficient over the 650 - 700 nm range, photons generated from the source within this energy range will result in photocarrier generation throughout the entire thickness of the film. The detectors were illuminated under 475 W m^{-2} white LED light for 1000 μs and the photo-CELIV measurements were conducted under several ramp rates/voltage rise speeds. **Figure 5**a displays the photo-charge extraction transient recorded for the HTLFD under a ramp rate of 1 V ms^{-1}. The photo-CELIV charge carrier mobility was estimated from the equation[34] given below:

$$\mu = \frac{2d^2}{3At_{max}^2\left[1+0.36\frac{Jmax-Jo}{Jo}\right]} \tag{4}$$

where μ is the charge carrier mobility, d is the detector active layer thickness, A is the ramp rate, J_{max} is the peak current, and J_o is the current plateau value at the end of the ramp. For the HTLFD, estimated carrier mobilities were in the range of 10^{-4} cm^2 V^{-1} s^{-1} to 10^{-3} cm^2 V^{-1} s^{-1} resulting in a mean mobility value of 2.9 × 10^{-4} cm^2 V^{-1} s^{-1}. Other detectors tested in this work also displayed a mobility value of similar magnitude (Figure S5, Supporting Information). These mobility values are in the same order as those reported for the previous generation of NP-BHJ X-ray detectors (~10^{-3} cm^2 V^{-1} s^{-1})[1] estimated from the Time-of-flight method as well as those reported for the P3HT: PC$_{70}$BM organic BHJ solar cells (6.4 × 10^{-4} cm^2 V^{-1} s^{-1})[34] estimated from the photo-CELIV method. While the photo-CELIV technique does not enable mobilities of electrons and holes to be extracted separately, the characteristic t_{max} depends predominantly on charge carrier type with the higher mobility.[34] However, the "square shaped" nature of the X-ray photocurrent transients observed (as opposed to a saw-tooth profile) indicates that both charge carriers possess similar mobilities.
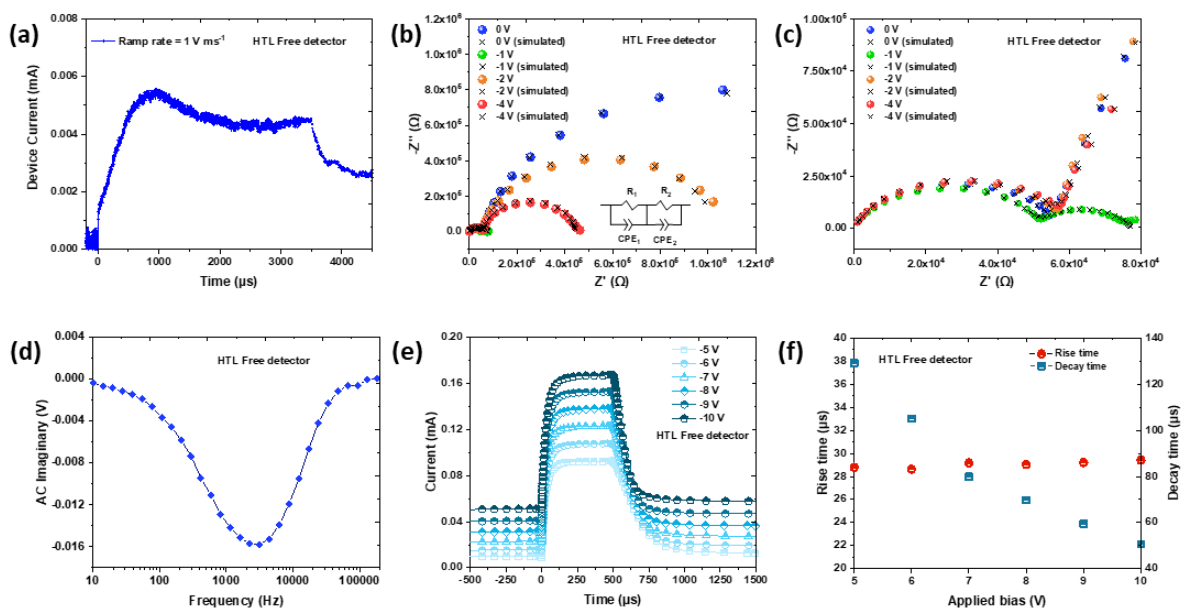
Figure 5. Charge carrier transport in NP-BHJ X-ray detectors. (a) Example photo-CELIV current transient of the HTLFD. (b) Nyquist plots for the HTLFD obtained under dark conditions when biased at 0, -1, -2, and -4 V. The black color crosses (×) represent the fits for each bias calculated using the equivalent circuit shown in the inset. R_1 and R_2 are resistance components forming a parallel circuit with the constant phase elements CPE_1 and CPE_2. (c) An expanded view of the Nyquist plots of the HTLFD displaying the smaller semicircle at frequencies above 15 kHz. (d) IMVS spectrum of the HTLFD from which, recombination lifetimes in the range of ~50 - 70 μs are estimated. (e) Photocurrent transients of the HTLFD under -5, -6, -7, -8, -9, and -10 V biases. (f) Rise time of the HTLFD plotted together with decay time, both as a function of applied bias. The decay time reduces with increasing voltage which is attributed to the field dependent mobility of carriers in organic semiconductors.

The charge carrier recombination lifetime of the detectors was estimated by conducting impedance spectroscopy (IS) (under dark conditions). The impedance spectra were acquired under four negative applied bias conditions (0, -1, -2, -4 V). Figure 5b shows the Nyquist plots for the HTLFD where two semicircles are observed; one at high frequencies above 15 kHz (Figure 5c) and the other one at lower frequencies below 15 kHz. Similar behavior was observed for detectors comprising NiO as the HTL (Figure S6, Supporting Information). The Nyquist plots were analyzed using an equivalent circuit shown in the inset of Figure 5b, consisting of R_1 and R_2 resistance components which form a parallel circuit with constant phase elements, CPE_1 and CPE_2. We attribute one semicircle to the top surface of the hybrid film which is enriched with P3HT phase and the other semicircle to the bottom region of the film consisting of Bi_2O_3 NPs, P3HT, and $PC_{70}BM$.[35] The adopted circuit model can describe the impedance

characteristics accurately, as seen by the agreement between the simulated curves and the impedance spectra across the whole frequency range. Furthermore, from the impedance spectra, two characteristic times associated with charge carrier transport can be extracted. The effective charge carrier lifetime (τ_n) from the peak position of the larger semicircle in the low frequency regime. Also, the charge carrier transit time (τ_d), from the transition point of the first semicircle to the second semicircle.[36] From the impedance spectra recorded at -2 and -4 V, we estimated the carrier lifetime to be in the range of ~3 to 13 ms for each detector type, irrespective of the hole selective condition. To evaluate the influence of an increased carrier density on the recombination lifetimes, we carried out intensity modulated photovoltage spectroscopy (IMVS) measurements. The recombination lifetimes estimated from the IMVS technique (Figure 5d and Figure S6, Supporting Information) were estimated to be between ~50 - 70 μs which is two orders of magnitude lower than that estimated using IS. This is in agreement with increased charge carrier recombination in the presence of a higher carrier density.[37]

In order to overcome the limitations associated with estimating rise time and decay time components using the X-ray photocurrent measurements, time constants of the NP-BHJ detectors were evaluated using the transient photocurrent (TPC) method as a function of applied bias. Each detector was illuminated with a 475 W m^{-2} white LED light for a duration of 500 μs and the photocurrent responses were recorded at biases ranging from -5 to -10 V. The photocurrent transients reported under each bias condition for the HTLFD are shown in Figure 5e. The photocurrent transients of the NP-BHJ X-ray detectors demonstrated rise time and decay time components in the microsecond time scales and therefore not observable in the X-ray photocurrent experiments. We observed that for each detector, the rise time does not change significantly with increasing negative applied bias, whereas the decay time of the detectors reduced with the increasing negative applied bias (Figure 5f and Figure S7, Supporting Information). This relationship between the decay time and the applied bias can be attributed to the field dependence of the charge carrier mobility in organic semiconductors leading to

increased charge carrier extraction under higher electric fields.[38] Overall, the rise times of the NiO-based detectors were ~23-24 μs whereas HTLFD showed a rise time of ~29 μs. Furthermore, the decay time of the HTLFD was approximately 50 μs when a bias of -10 V was applied. Such decay times are comparable to that of the high purity Germanium detectors which have been reported to display decay times in the order of 10 μs.[39] The relatively fast response times of the optimized NP-BHJ detectors indicate that very low trap states exist at the anode/NP-BHJ interface and that any bulk traps existing within the organic-inorganic hybrid layer are relatively shallow.[17]

2.6. Dosimetric Characterization of NP-BHJ X-Ray Detectors for Radiotherapy

One possible application of these NP-BHJ X-ray detectors would be as a dosimeter for dose mapping during radiotherapy. Conventional radiotherapy techniques such as Intensity Modulated Radiotherapy (IMRT) and Volumetric Modulated Arch Therapy (VMAT) require precise dosimeters to accurately monitor incident dose, exit dose and dose distributions during verification measurements to confirm accuracy of radiotherapy treatment delivery.[40] Therefore, we expanded our investigations to evaluate the dosimetric performance of the HTLFDs under exposure to hard X-rays from a 6 MV clinical linear accelerator (**Figure 6**a, b). We note that a calibrated ionization chamber was placed adjacent to our detector (Figure 6b) for all measurements other than the angular dependence studies. This allows the identification of enhancement effects on the X-ray photocurrent from the detector due to the high energy X-ray interaction with the device electrodes, scattering from the patient treatment couch etc. No deviation in the ionization chamber response was observed from its calibrated values, which indicates that the responses observed here are not influenced from any extrinsic effects. Any enhancement effects from the test clips used for carrying the charges from the device electrodes to the measurement unit used were also mitigated by designing the contact architecture such that the clip is placed away from the active pixel area.
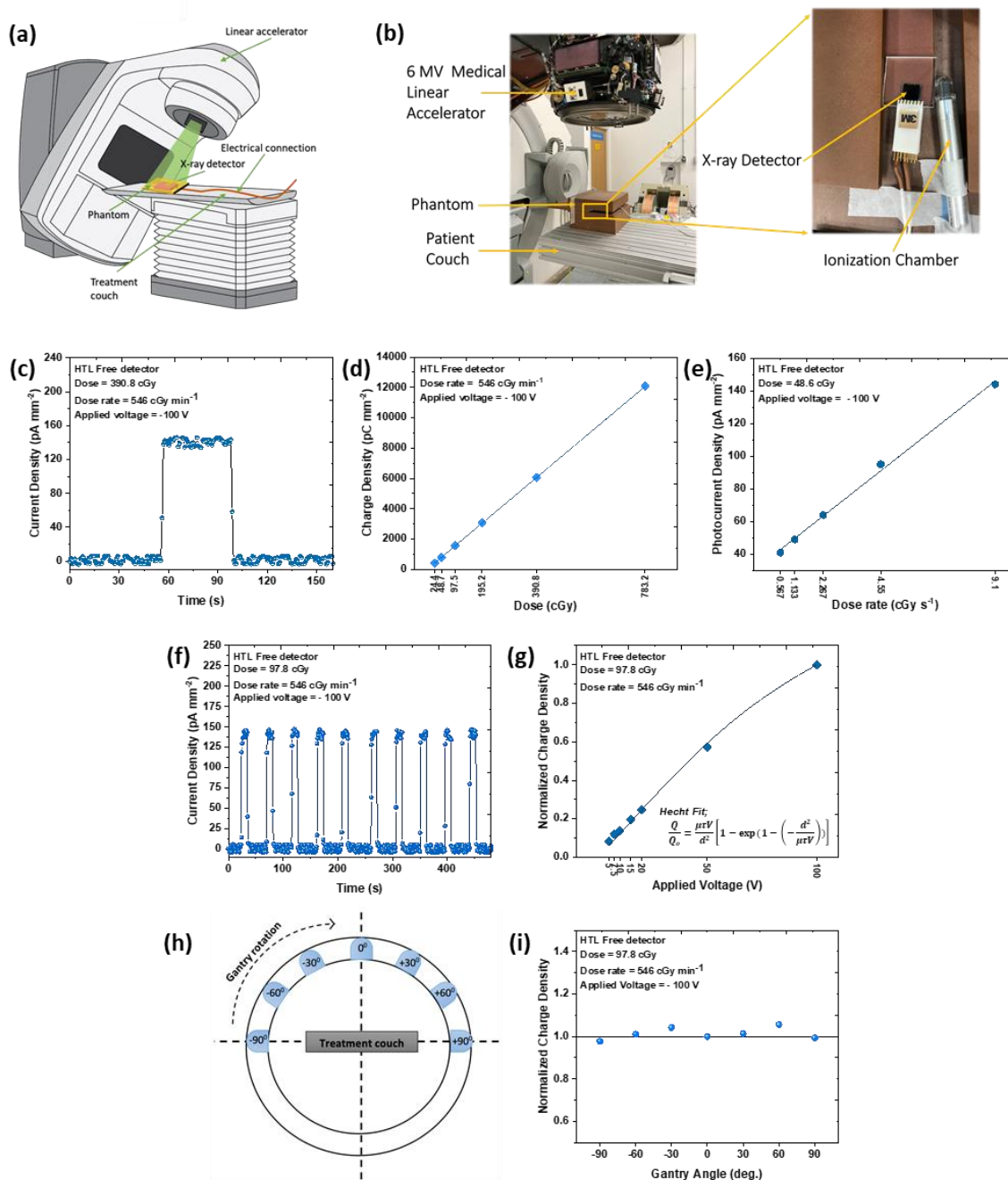
Figure 6. Response characteristics of the HTL Free detector under the 6 MV hard X-rays. (a) Schematic of the experimental arrangement used for detector characterization under 6 MV hard X-ray radiation. Schematic for LINAC adapted from https://www.cancer.ca/. (b) An enlarged view of the experimental arrangement emphasizing the configuration of the detector, ionization chamber, and the phantom. (c) X-ray photocurrent response from the detector. (d) Dose and, (e) Dose rate dependence of the HTLFD showing excellent linearity ($R^2 > 0.9998$). (f) Reproducibility of the response characteristics under repeated X-ray exposure. (g) Voltage dependence of the detector together with the Hecht fit ($R^2 > 0.9998$) for estimation of the $\mu\tau$ product. (h) Schematic diagram illustrating the gantry angle rotation of the linear accelerator. (i) Beam angle dependence of the detector showing less than 6% variation in detector response with beam incidence angle. Data points in Figures (d), (e), (g), (i) are averaged over three measurements.

Analogous to the response characteristics observed under 70 kV X-ray radiation, we observed a sharp rise and decay in X-ray photocurrent response with a "square shaped" photo transient (Figure 6c). The HTLFDs also displayed an excellent dose linearity and dose rate linearity as shown in the Figure 6d and e, respectively. The sensitivity of the detector estimated from the dose dependence method was ~1.5 mC Gy^{-1} cm^{-2} which is the highest reported for an organic or hybrid detector at this energy range. We note that this sensitivity value is an improvement by ~×100 higher than our previous generation of NP-BHJ detectors (~60 μC Gy^{-1} cm^{-2}) which was previously reported to possess the highest sensitivity for semiconductor detectors tested under a 6 MV LINAC.[1] This increased sensitivity is attributed to the higher dose, applied bias, and the X-ray energy applied to this detector. Even though the expected X-ray attenuation is poor at high energies, it should be noted that Compton scattering becomes dominant in this energy range, therefore resulting in an electron cascade contributing towards a very high sensitivity.[41] Our detectors also displayed very high reproducibility under the repeated X-ray exposures, with a maximum deviation of only 2.8% as shown in Figure 6f. The voltage dependence of the HTLFDs under hard X-ray radiation was studied by applying a bias ranging from -5 V to -100 V. The trend between the charge density and applied voltage was fitted to the Hecht equation (Figure 6g) yielding a μτ product of ~1.8 × 10^{-7} cm^2 V^{-1} which is comparable to the result obtained from the voltage dependence studies under 70 kV soft X-ray radiation.

During IMRT and VMAT, the gantry head of the linear accelerator is rotated around the body for the beam delivery from specific angles to the target volume consisting of the tumor and appropriate margin to account for possible microscopic spread and geometric uncertainties arising from internal patient motion and patient set up.[40] Therefore, in such a scenario, a dosimeter must be able to accurately measure the dose irrespective of the beam angle/gantry angle. In order to evaluate the angular dependence of the detector response, we carried out X-ray photocurrent measurements by varying the gantry angle of the linear accelerator from -90° to +90° (Figure 6h). We observed a slight dependence of the photocurrent response of the

detector on the beam angle, particularly at intermediate angles between 0° and ±90°. The quantitative analysis of the normalized charge density generated at each angle to the charge density at 0° indicates a maximum deviation of 5.6 % (at +60°) (Figure 6i). This value is significantly lower compared to the angular dependencies reported from commercial diode detectors which showed a maximum deviation of about 21 %.[42]

3. Conclusion

We have developed HTL Free organic-inorganic hybrid X-ray detectors with ultra-low dark currents below 10 pA mm^{-2} under electric fields as high as ~4 V μm^{-1}, irrespective of the P3HT *Mw* or the NP-BHJ layer thickness used. This was identified to be due to the vertical phase separation induced within the BHJ thereby resulting in an internal hole selective mechanism. Such X-ray detectors fabricated without an HTL displayed very appealing characteristics such as dose linearity, dose rate linearity, and reproducibility not only under 70 kV soft X-ray radiation but also under 6 MV hard X-ray radiation with an exceptionally high sensitivity of ~1.5 mC Gy^{-1} cm^{-2}. The above-mentioned characteristics combined with the ultra-low dark currents, high sensitivity, low beam angle dependence, and also long-term stability with regards to maintaining both the low dark currents as well as detector sensitivity indicate that these detectors are promising candidates for dosimetry in radiotherapy, medical imaging as well as industrial applications. We anticipate detector response characteristics comparable to the conventional X-ray detectors with added benefits of flexibility and much lower cost, through engineering of the detector for optimized charge transport within the active matrix. This would stimulate further interest towards NP-BHJ composites for X-ray detection in a diverse range of applications including in remote areas with lower resources and power budgets.

4. Experimental Section/Methods
Solution preparation: Regioregular Poly(3-hexylthiophene-2,5-diyl) (P3HT; 80 mg; *Mw* 52 kDa; Regioregularity 91%; Rieke 4002-EE), [6,6]-Phenyl C71 butyric acid methyl ester

(PC$_{70}$BM; 80 mg; purity > 99%; Solenne), and Bi$_2$O$_3$ NPs (80 mg; β phase with a tetragonal crystal structure; 38 nm diameter; surface area 18 m^2 g^{-1}; Alfa Aesar) were added to Dichlorobenzene (DCB; 1 mL; anhydrous; Sigma-Aldrich) and stirred overnight to produce P3HT: PC$_{70}$BM: Bi$_2$O$_3$ solution for NiO-based detector fabrication. P3HT: PC$_{70}$BM: Bi$_2$O$_3$ solutions with different concentration ratios (20mg: 20mg: 20mg, 40mg: 40mg: 40mg, 60mg: 60mg: 60mg, 80mg: 80mg: 80mg) in DCB (1 mL) were prepared to fabricate detectors with NP-BHJ layer thickness 10, 25, 40, 55 μm, respectively. NP-BHJ detectors with different P3HT *Mw* s were fabricated by using 91% regioregular P3HT (Rieke 4002-EE) with *Mw*s of 37, 52, and 64 kDa for the P3HT: PC$_{70}$BM: Bi$_2$O$_3$ (80mg: 80mg: 80mg in 1 mL of DCB). The solutions were preheated at 60 °C while stirring for 30 min before deposition of the films. The solution preparation was carried out in a N$_2$ glove box (MBraun MB20G).

Device fabrication: Devices were fabricated on ITO (In$_2$O$_3$: Sn) glass substrates (15 mm × 15 mm, 15 Ω per square, Luminescence Technology Corp.). An electron transporting Aluminium-doped Zinc Oxide (ZnO) NP dispersion (Sigma-Aldrich) layer was spin coated in air (3000 rpm for 30 s) and annealed at 80°C for 10 min to give a thickness of 40 nm. P3HT: PC$_{70}$BM: Bi$_2$O$_3$ solution was then casted. Devices were annealed (at 60 °C) for ~60 min in air, until a relatively dry layer was obtained. After the low temperature annealing process, devices were annealed at 140°C for 10 min in a N$_2$ glove box (MBraun MB20G). Devices were kept under vacuum at a pressure of less than 3 × 10^{-3} mbar for 48 h to remove any residual solvent. This was followed by deposition of the hole transport layer; for NiO-based devices, each concentration of NiO (2.5, 1.25, 0.63, 0.31, and 0.16 wt. % in Ethanol; Avantama) was spin coated in air (at 1500 rpm for 30 s). For HTL Free devices, no external HTL was deposited. This was followed by the deposition of the silver anode (~120 nm) by thermal evaporation.

X-ray irradiation and characterization: For each detector, three measurements were recorded under each irradiation condition. Detector response was characterized under both soft and hard X-ray radiation;

(1) A 70 kV microfocus X-ray source (Hamamatsu L6732-01) under a dose rate range of 0.67027 – 2.7510 cGy s^{-1}. A Keithley 2410 source measurement unit was used for recording the electrical characteristics. A dosimeter (Farmer 2670, Thermo Fisher Scientific) in combination with an ionization chamber (2611A, Thermo Fisher Scientific) was used for measurement of dose rates. The dose rates were then calculated for the pixel area of the devices (0.68 cm^2).

(2) 6 MV X-rays from a clinical linear accelerator (Elekta Synergy) located at the National Physical Laboratory (NPL). Dose rates from 34 cGy min^{-1} to 546 cGy min^{-1} were provided by the LINAC and a Keithley 2400 source measurement unit was used for recording electrical characteristics of the devices. A calibrated ionization chamber (N.E. TECH/N.P.L. TYPE 2611A Ser. No. 122) was used to eliminate unintended X-ray photocurrent enhancement.

For measurements carried out under both above sources, the response of the devices was normalized to the pixel area as defined by the electrode overlap (between Ag and ITO) of 0.68 cm^2.

TGA: Thermogravimetric analysis of the NP-BHJ film was carried out under air, using a thermogravimetric analyzer (Q500 V6.7; TA Instruments). The sample was heated from room temperature to 700 °C at a heating rate of 10 °C min^{-1}.

Atomic Force Microscopy: Glass/ITO/NP-BHJ/NiO samples were prepared as stated earlier. The surface roughness of each NiO coated hybrid film was evaluated by using an AIST-NT

atomic force microscope. The experiment was conducted in the tapping mode. The RMS roughness of the films was evaluated using the Gwyddion software.

SKPM: Glass/ITO/NP-BHJ samples were prepared as stated earlier. The surface potential of the NP-BHJ film was evaluated by amplitude-modulated 2-pass scanning Kelvin probe microscopy (Combiscope 1000; AIST-NT). The work function of the tip was calibrated on highly ordered pyrolytic graphite (HOPG) before and after the measurement on the hybrid film to account for drift due to adsorbed water. The measurements were conducted in dry nitrogen, with oxygen and water below 1 ppm.

Cross-sectional Imaging: Samples were prepared by fabrication of the NP-BHJ film on the ITO coated glass substrates as described earlier. Cross sectional morphology of the NP-BHJ film was examined using a FERA3; TESCAN dual beam/focused ion beam scanning electron microscope under an accelerating voltage of 5 kV.

ToF-SIMS: Glass/ITO/NP-BHJ samples were prepared as stated earlier. Time-of-flight secondary ion mass spectrometry was used for depth profiling of the NP-BHJ film using a TOF.SIMS 5 (IONTOF GmbH) instrument with 30 keV Bi_3^+ ions for analysis and $Ar_{1700-2000}^+$ ions at 20 keV for sputtering in non-interlaced mode. Low-energy electrons were used to flood the surface during the measurements. The sputter beam was rasterized in random mode over a $250 \times 250 \ \mu m^2$ area with the analysis area of $50 \times 50 \ \mu m^2$. Every plane of the analyzed volume was rasterized in random mode with 128×128 pixels at 1 shot per pixel and 3 frames following by 7 frames of sputtering. The instrument was operated in the negative ion polarity.

Data acquisition was obtained using SurfaceLab software (IONTOF GmbH). Depth profiles were exported using the ASCII export function and 3D maps were exported using the 3D Rendering function.

GIWAXS: Glass/ITO/NP-BHJ samples were prepared as stated earlier. GIWAXS measurements were performed using a Xeuss 2.0 (Xenocs, France) system equipped with a liquid gallium MetalJet source (Excillum, Sweden) which provides a 9.243 keV X-ray beam. The beam was collimated to a spot of with a lateral dimension of 400 μm on the sample. A Pilatus3R 1M 2D detector (Dectris, Switzerland) placed at ∼307 mm from the sample was used to obtain the diffraction images with both the sample chamber and flight tubes held under vacuum to remove background air scatter. Calibration of the sample-to-detector distance was carried out using a silver behenate calibrant in transmission geometry, while GIWAXS measurements were performed at incident angles of 0.05°, 0.1°, 0.2°, and 0.3°. This data was corrected, reduced and reshaped using the GIXSGUI MATLAB toolbox.[43]

Parameters for the Scherrer formula were extracted from Gaussian curve fittings of the P3HT (100) peak using OriginPro software.

Drop shape analysis: Glass/ITO/NP-BHJ, Glass/ITO/P3HT, and Glass/ITO/PC$_{70}$BM samples were prepared as stated earlier. The contact angle was determined from the shadow image of a sessile drop of water by using the drop shape analyzer (DSA25, KRÜSS GmbH). The surface free energy of each film was estimated from the ADVANCE software by using three contact angle measurements.

Photo-CELIV, IS, IMVS, and TPC: The Photo-CELIV, impedance spectroscopy, intensity modulated photovoltage spectroscopy, and transient photocurrent measurements were conducted using the Paios 4 all-in-one test platform by FLUXiM (Paios 4, Platform for all-in-one characterization of solar cells and OLEDs, Fluxim AG 2019, https://www.fluxim.com/paios). Devices were fabricated using the same methodology described for X-ray response characterization. The pixel area was reduced to 3 mm^2 in order to minimize capacitive effects that can influence device characteristics.

References

[1]   H. M. Thirimanne, K. D. G. I. Jayawardena, A. J. Parnell, R. M. I. Bandara, A. Karalasingam, S. Pani, J. E. Huerdler, D. G. Lidzey, S. F. Tedde, A. Nisbet, C. A. Mills, & S. R. P. Silva, *Nat. Commun*. **2018,** 9, 2926.

[2]   A. Ciavatti, L. Basiricò, I. Fratelli, S. Lai, P. Cosseddu, A. Bonfiglio, J. E. Anthony, B. Fraboni, *Adv. Funct. Mater.* **2019**, *29*, 1806119.

[3]   A. Intaniwet, C. A. Mills, M. Shkunov, P. J. Sellin, J. L. Keddie, *Nanotechnology*. **2012,** 23, 235502.

[4]   C. A. Mills, H. Al-Otaibi, A. Intaniwet, M. Shkunov, S. Pani, J. L. Keddie, P. J. Sellin, *J. Phys. D Appl. Phys*. **2013,** 46, 275102.

[5]   A. Ciavatti, T. Cramer, M. Carroli, L. Basiricò, R. Fuhrer, D. M. De Leeuw, B. Fraboni, *Appl. Phys. Lett*. **2017,** 111, 183301.

[6]   P. Büchele, M. Richter, S. F. Tedde, G. J. Matt, G. N. Ankah, R. Fischer, M. Biele, W. Metzger, S. Lilliu, O. Bikondoa, J. E. Macdonald, C. J. Brabec, T. Kraus, U. Lemmer, O. Schmidt, *Nat. Photonics* **2015**, *9*, 843.

[7]   K. D. G. I. Jayawardena, H. M. Thirimanne, S. F. Tedde, J. E. Huerdler, A. J. Parnell, R. M. I. Bandara, C. A. Mills, S. R. P. Silva, *ACS Nano* **2019**, *13*, 6973.

[8]   J. B. Frey, G. Belev, O. Tousignant, H. Mani, L. Laperriere, S. O. Kasap, *J. Appl. Phys.* **2012**, *112*.

[9]   J. Ohshita, Y. Tada, A. Kunai, Y. Harima, Y. Kunugi, *Synth. Met.* **2009**, *159*, 214.

[10]   M. P. De Jong, L. J. Van Ijzendoorn, M. J. A. De Voigt, *Appl. Phys. Lett.* **2000**, *77*, 2255.

[11]   K. D. G. I. Jayawardena, S. Li, L. F. Sam, C. T. G. Smith, M. J. Beliatis, K. K. Gandhi, M. R. R. Prabhath, T. R. Pozegic, S. Chen, X. Xu, G. D. M. R. Dabera, L. J. Rozanski, R. A. Sporea, C. A. Mills, X. Guo, S. R. P. Silva, *Nanoscale* **2015**, *7*, 14241.

[12]   F. A. Boroumand, M. Zhu, A. B. Dalton, J. L. Keddie, P. J. Sellin, J. J. Gutierrez, **2007**.

[13] A. Intaniwet, J. L. Keddie, M. Shkunov, P. J. Sellin, *Org. Electron*. **2011,** 12, 1903-1908.

[14] A. Ciavatti, E. Capria, A. Fraleoni-Morgera, G. Tromba, D. Dreossi, P. J. Sellin, P. Cosseddu, A. Bonfiglio, B. Fraboni, *Adv. Mater.* **2015**, *27*, 7213.

[15] L. Basirico, A. Ciavatti, M. Sibilia, A. Fraleoni-Morgera, S. Trabattoni, A. Sassella, B. Fraboni, *IEEE Trans. Nucl. Sci.* **2015**, *62*, 1791.

[16] G. H. Gelinck, A. Kumar, D. Moet, J. L. P. J. Van Der Steen, A. J. J. M. Van Breemen, S. Shanmugam, A. Langen, J. Gilot, P. Groen, R. Andriessen, M. Simon, W. Ruetten, A. U. Douglas, R. Raaijmakers, P. E. Malinowski, K. Myny, *IEEE Trans. Electron Devices* **2016**, *63*, 197.

[17] Y. C. Kim, Y. S. Choi, S. Y. Lee, **2017**.

[18] S. Shrestha, R. Fischer, G. J. Matt, P. Feldner, T. Michel, A. Osvet, I. Levchuk, B. Merle, S. Golkar, H. Chen, S. F. Tedde, O. Schmidt, R. Hock, M. Rührig, M. Göken, W. Heiss, G. Anton, C. J. Brabec, *Nat. Photonics* **2017**, *11*, 436.

[19] W. Pan, H. Wu, J. Luo, Z. Deng, C. Ge, C. Chen, X. Jiang, W.-J. Yin, G. Niu, L. Zhu, L. Yin, Y. Zhou, Q. Xie, X. Ke, M. Sui, J. Tang, *Nat. Photonics* **2017**, *11*, 726.

[20] W. Wei, Y. Zhang, Q. Xu, H. Wei, Y. Fang, Q. Wang, Y. Deng, T. Li, A. Gruverman, L. Cao, J. Huang, *Nat. Photonics* **2017**, *11*, 315.

[21] Z. Gou, S. Huanglong, W. Ke, H. Sun, H. Tian, X. Gao, X. Zhu, D. Yang, P. Wangyang, *Phys. status solidi – Rapid Res. Lett.* **2019**, *13*, 1900094.

[22] H. Mescher, E. Hamann, U. Lemmer, *Sci. Rep.* **2019**, *9*, 1.

[23] L. Li, F. Zhang, J. Wang, Q. An, Q. Sun, W. Wang, J. Zhang, F. Teng, *Sci. Rep.* **2015**, *5*, 1.

[24] L. Basiricò, A. Ciavatti, T. Cramer, P. Cosseddu, A. Bonfiglio, B. Fraboni, *Nat. Commun.* **2016**, *7*, 13063.

[25] N. Koenigsfeld, R. Kalish, A. Cimmino, D. Hoxley, S. Prawer, I. Yamada, *Appl. Phys.*

Lett. **2001**, *79*, 1288.

[26]   H. Bristow, P. Jacoutot, A. D. Scaccabarozzi, M. Babics, M. Moser, A. Wadsworth, T.

       D. Anthopoulos, A. Bakulin, I. McCulloch, N. Gasparini, *ACS Appl. Mater. Interfaces*

       2020.

[27]   A. Adams, F. Nicol, S. McHugh, J. Moore, G. Matis, G. A. Amparan, In *Infrared*

       Imaging Systems: Design, Analysis, Modeling, and Testing XXX; Krapels, K. A.; Holst,

       G. C., Eds.; SPIE, **2019**; Vol. 11001, p. 28.

[28]   S. O. Kasap, J. A. Rowlands, *J. Mater. Sci. Mater. Electron.* **2000**, *11*, 179.

[29]   J. Yuan, T. Huang, P. Cheng, Y. Zou, H. Zhang, J. L. Yang, S. Y. Chang, Z. Zhang, W.

       Huang, R. Wang, D. Meng, F. Gao, Y. Yang, *Nat. Commun.* **2019**, *10*, 1.

[30]   V. S. Smentkowski, G. Zorn, A. Misner, G. Parthasarathy, A. Couture, E. Tallarek, B.

       Hagenhoff, *Cite as J. Vac. Sci. Technol. A* **2013**, *31*, 30601.

[31]   J. Als-Nielsen, D. Mcmorrow, *Elements of Modern X-ray Physics Second Edition*.

[32]   M. L. Chabinyc, *Polym. Rev.* **2008**, *48*, 463.

[33]   M. Kim, J. Lee, S. B. Jo, D. H. Sin, H. Ko, H. Lee, S. G. Lee, K. Cho, *J. Mater. Chem.*

       A **2016**, *4*, 15522.

[34]   M. Stephen, K. Genevičius, G. Juška, K. Arlauskas, R. C. Hiorns, *Polym. Int.* **2017**, *66*,

       13.

[35]   E. Von Hauff, **2019**.

[36]   J. Bisquert, *J. Phys. Chem. B* **2002**, *106*, 325.

[37]   F. Laquai, D. Andrienko, C. Deibel, D. Neher, *Advances in Polymer Science*. **2017,**

       272, 267–291.

[38]   S. Bange, M. Schubert, D. Neher, *Phys. Rev. B - Condens. Matter Mater. Phys.* **2010**,

       81, 035209.

[39]   P. Jansson, *Digital Pulse Processing in HPGe Gamma-Ray Spectroscopy Courses on*

   *Activity Measurements with Germanium Detectors* **2016**.

[40]   M. Hussein, E. J. Adams, T. J. Jordan, C. H. Clark, A. Nisbet, *J. Appl. Clin. Med. Phys.* **2013**, *14*, 274.

[41]   J. T. Bushberg, J. A. Seibert, E. M. Leidholdt, J. M. Boone, E. J. Goldschmidt, *Med. Phys.* **2003**, *30*, 1936.

[42]   D. Marre, G. Marinello, *Med. Phys.* **2004**, *31*, 50.

[43]   Z. Jiang, *J. Appl. Crystallogr.* **2015**, *48*, 917.

ToC description:

Organic-Inorganic hybrid systems are a promising class of materials for X-ray detection. However, their performance has been restricted by high dark currents. This work introduces a methodology to achieve hybrid X-ray detectors with ultra-low dark currents through enrichment of the p-type semiconductor at the absorber/anode interface.

M. Prabodhi A. Nanayakkara, Lidija Matjacic, Sebastian Wood, Filipe Richheimer, Fernando A. Castro, Sandra Jenatsch, Simon Züfle, Rachel Kilbride, Andrew J. Parnell, Mateus G. Masteghin, Hashini M. Thirimanne, Andrew Nisbet, K. D. G. Imalka Jayawardena, S. Ravi P. Silva*

Ultra-Low Dark Current Organic-Inorganic Hybrid X-Ray Detectors
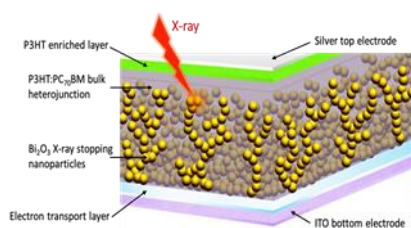
Organic-inorganic hybrid X-ray detectors with dark currents < 10 pA mm^2

Supporting Information

Ultra-Low Dark Current Organic-Inorganic Hybrid X-Ray Detectors

M. Prabodhi A. Nanayakkara, Lidija Matjacic, Sebastian Wood, Filipe Richheimer, Fernando A. Castro, Sandra Jenatsch, Simon Züfle, Rachel Kilbride, Andrew J. Parnell, Mateus G. Masteghin, Hashini M. Thirimanne, Andrew Nisbet, K. D. G. Imalka Jayawardena, S. Ravi P. Silva*

M. P. A. Nanayakkara, M. G. Masteghin, Dr H. M. Thirimanne, Dr K. D. G. I. Jayawardena, Prof. S. R. P. Silva
Department of Electrical and Electronic Engineering, Advanced Technology Institute, University of Surrey, Guildford, Surrey, GU2 7XH, United Kingdom.
E-mail: s.silva@surrey.ac.uk

Dr L. Matjacic, Dr S. Wood, F. Richheimer, Dr F. A. Castro
National Physical Laboratory, Teddington, Middlesex, TW11 0LW, UK.

Dr S. Jenatsch, Dr S. Züfle
FLUXiM AG, Katharina-Sulzer-Platz 2, 8400 Winterthur, Switzerland.

R. Kilbride, Dr A. J. Parnell
Department of Physics and Astronomy, University of Sheffield, Hicks Building, Sheffield, S3 7RH, UK.

Prof. A. Nisbet
Department of Medical Physics and Biomedical Engineering, University College London, Gower St, Bloomsbury, London WC1E 6BT, UK.

Note S1. Response characteristics of NiO-based detectors under the 70 kV X-ray radiation

NiO-based detectors also displayed stable and low dark current response of between 0.31-0.42 pA mm^{-2} at -10 V which appeared to be within the industrial standard even at an applied bias as high as -200 V (**Figure S3**). Similar to the HTL Free detectors, the NiO-based detectors demonstrated a "square shaped" X-ray photocurrent response (Figure S3a). The detectors also demonstrated excellent dose linearity (Figure S3b) and dose rate linearity (Figure S3c) resulting in sensitivity values of 23.1-24.9 nC Gy^{-1} cm^{-2} at -10 V and 60-62 nC Gy^{-1} cm^{-2} at -200 V which are comparable to the sensitivities observed from HTLFDs. The NiO-based detectors also demonstrated a reproducible X-ray photocurrent response (Figure S3d) with the maximum deviation of each detector being less than 3.5%. Furthermore, Hecht analysis carried out on each detector (Figure S3e) resulted in a μτ value of ~10^{-7} cm^2 V^{-1}. The SNR of detectors displayed a decaying characteristic (Figure S3f) due to the increase in dark current with voltage, similar to that observed for devices without an HTL. This is again attributed to the linear increase in dark current with voltage as opposed to the saturation of X-ray photocurrent with increasing voltage (Figure S4).
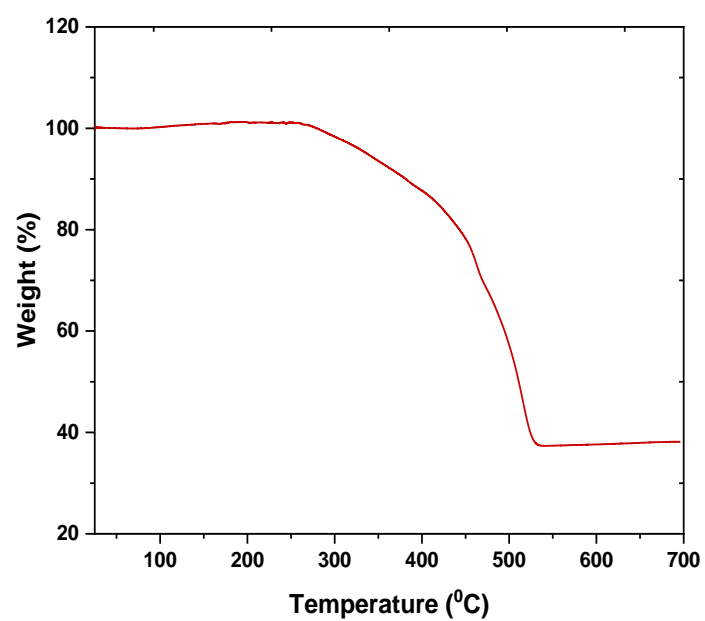
Figure S1. Determination of Bi_2O_3 NP weight percentage within the NP-BHJ film using thermogravimetric analysis. The estimated weight percentage of NPs is 38.1%.
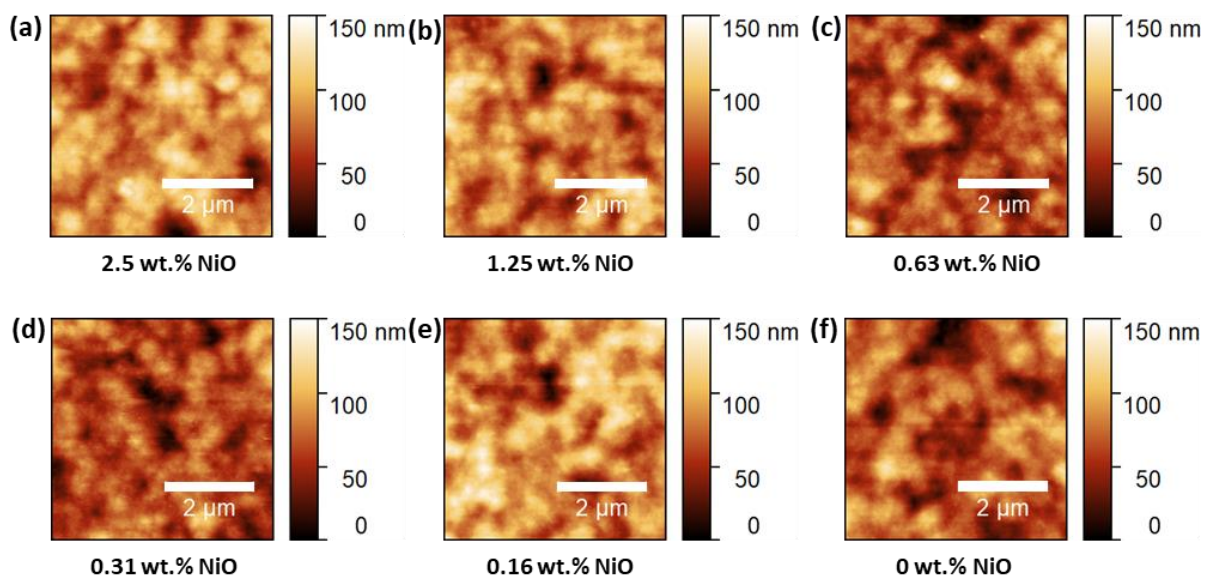
Figure S2. Effect of NiO concentration on the surface roughness of the NP-BHJ film. AFM micrographs of the organic-inorganic hybrid layer, when spin coated with (a) 2.5 wt. %, (b) 1.25 wt.%, (c) 0.63 wt.%, (d) 0.31 wt.%, (e) 0.16 wt.%, and (f) 0 wt. % NiO dispersion. No significant variation in the root mean square surface roughness was observed irrespective of the NiO concentration.
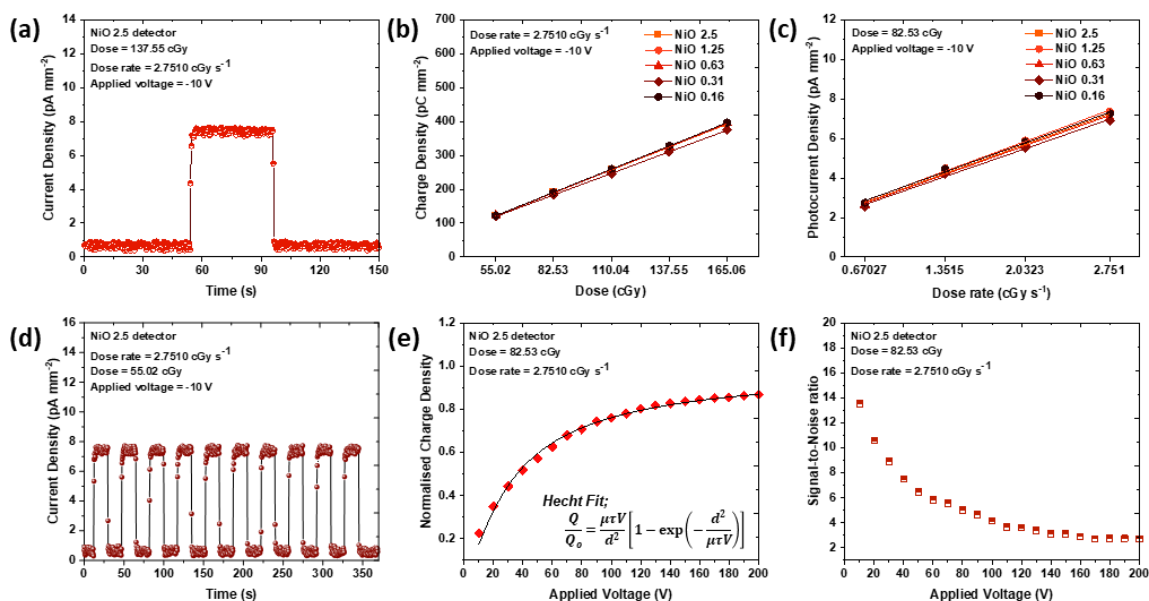
Figure S3. Response characteristics of the NiO-based detectors under 70 kV X-rays. (a) Transient X-ray photocurrent response from the NiO 2.5 detector indicating a "square shaped" response. (b) Dose and, (c) Dose rate dependence for the NiO-based detectors. The solid lines indicate linear fits. Both the dose as well as dose rate dependence shows excellent linearity (R^2 > 0.9998). (d) Reproducibility of the X-ray photocurrent response of the NiO 2.5 detector under repeated X-ray exposures. (e) Voltage dependence of the NiO 2.5 detector together with the Hecht fit (R^2 > 0.9998) for estimation of the μτ product. (f) SNR variation with applied bias of the NiO 2.5 detector. Data points in Figures (b), (c), (e), (f) are averaged over three measurements.
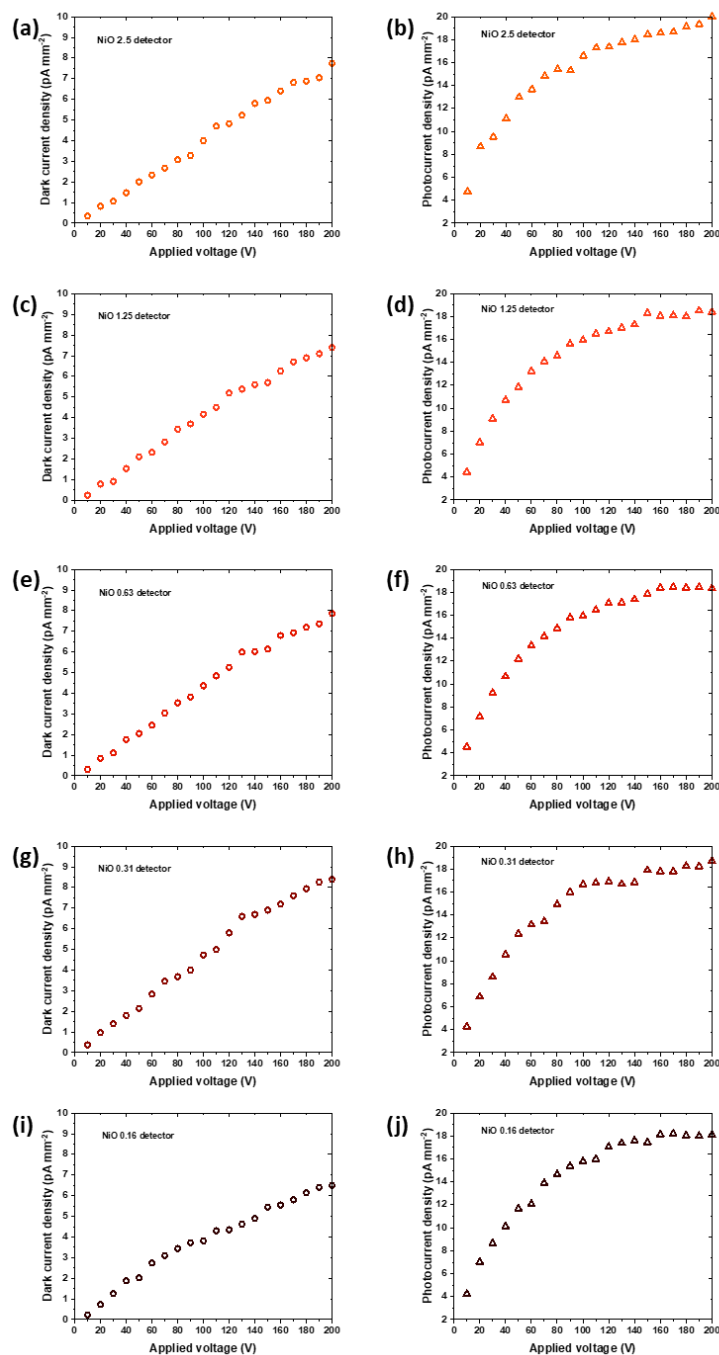
Figure S4. Voltage dependent dark current and photocurrent response characteristics of NiO-based detectors. The dark current density of the (a) NiO 2.5 detector, (c) NiO 1.25 detector, (e) NiO 0.63 detector, (g) NiO 0.31 detector, and (i) NiO 0.16 detector as a function of applied bias. The photocurrent density of the (b) NiO 2.5 detector, (d) NiO 1.25 detector, (f) NiO 0.63 detector, (h) NiO 0.31 detector, and (j) NiO 0.16 detector as a function of applied bias.
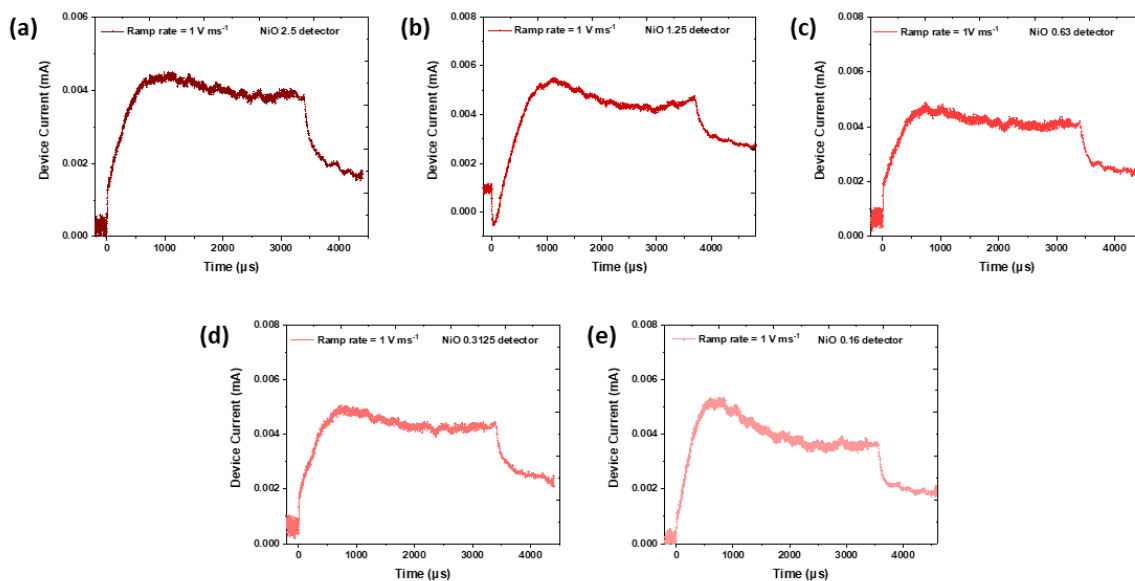
Figure S5. Charge carrier mobility estimation using photo-CELIV method. Current transient of the (a) NiO 2.5 detector, (b) NiO 1.25 detector, (c) NiO 0.63 detector, (d) NiO 0.31 detector, and (e) NiO 0.16 detector measured using the photo-CELIV technique under a ramp rate of 1 V ms^{-1} after a 1000 µs light pulse at 475 Wm^{-2} intensity.
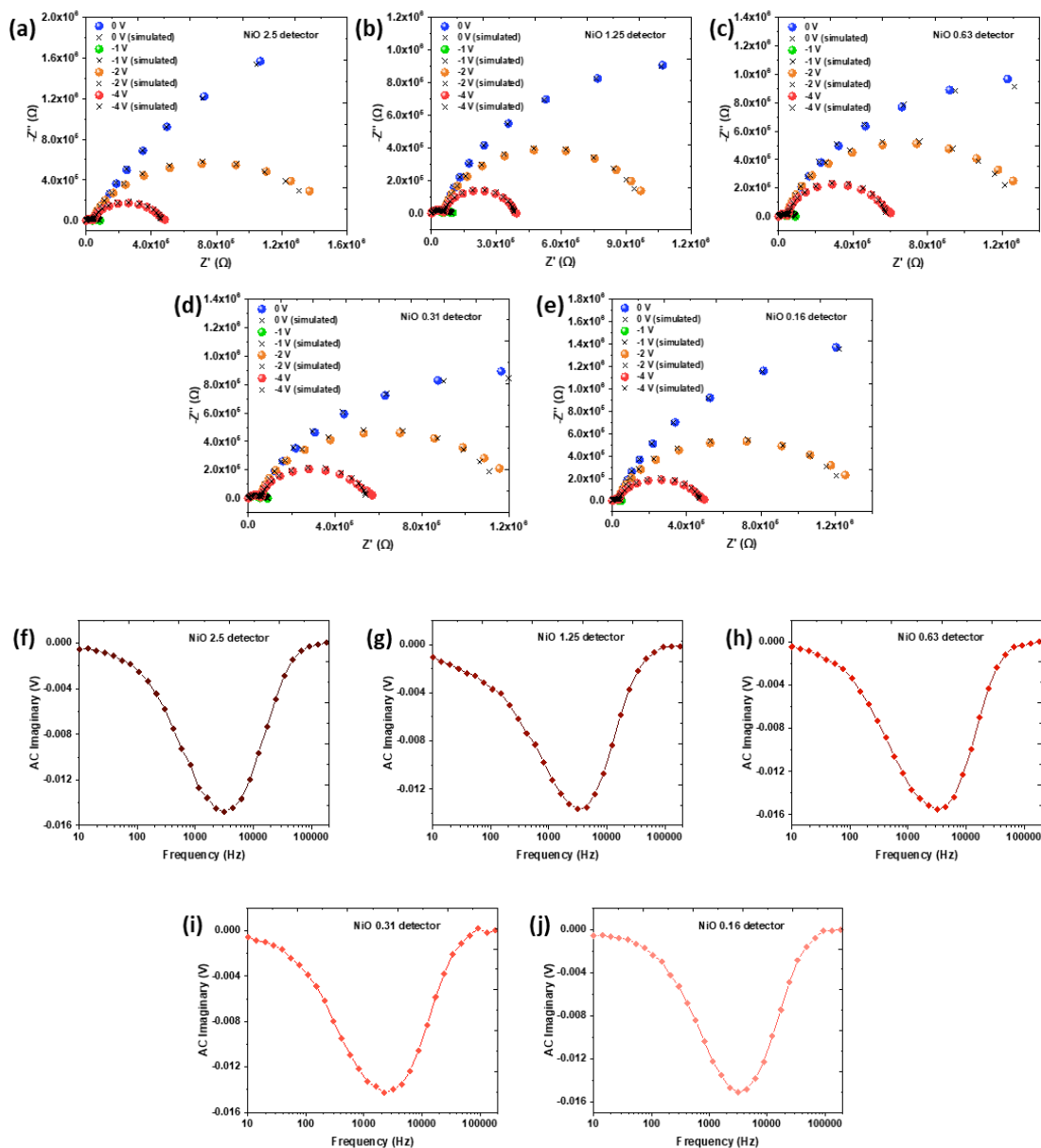
Figure S6. Charge carrier lifetime estimation using IS and IMVS methods. Nyquist plots for the (a) NiO 2.5 detector, (b) NiO 1.25 detector, (c) NiO 0.63 detector, (d) NiO 0.31 detector, and (e) NiO 0.16 detector obtained under dark conditions when biased at 0, -1, -2, and -4 V. The black color crosses represent the fitting curves under each applied bias. IMVS spectra for the (f) NiO 2.5 detector, (g) NiO 1.25 detector, (h) NiO 0.63 detector, (i) NiO 0.31 detector, and (j) NiO 0.16 detector. The illumination intensity is approx. 90% of the maximum (475 W m^{-2}), and the modulation amplitude is 10%.
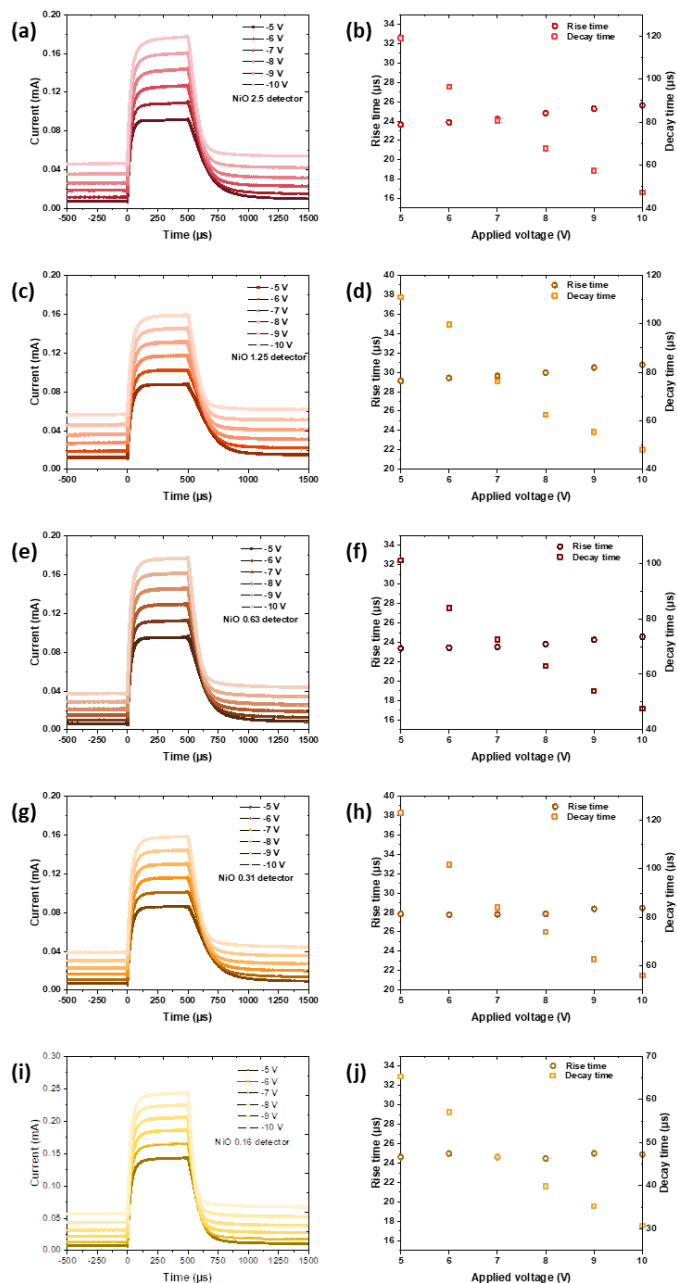
Figure S7. Rise and decay time estimation using the TPC method. Photocurrent transients of the (a) NiO 2.5 detector, (c) NiO 1.25 detector, (e) NiO 0.63 detector, (g) NiO 0.31 detector, and (i) NiO 0.16 detector under an applied bias from -5 V to -10 V when illuminated under the maximum light intensity for 500 μs. Corresponding rise and decay times of the (b) NiO 2.5 detector, (d) NiO 1.25 detector, (f) NiO 0.63 detector, (h) NiO 0.31 detector, and (j) NiO 0.16 detector as a function of applied bias.

Table S1. RMS roughness value observed under different NiO concentrations.

NiO concentration (wt. %)	RMS Surface roughness (nm)
2.5	21
1.25	20
0.63	21
0.31	18
0.16	23
0	21

Table S2. Variation of d-spacing, FWHM, and crystallite size with the incident angle for the

NP-BHJ film. Parameters have been estimated using GIWAXS data.

Angle (°)	d-spacing ($2\pi/Q$) (nm)	FWHM β (degrees)	Crystallite size D (nm)
0.05	1.60	0.489	14.7
0.1	1.61	0.452	15.9
0.2	1.61	0.452	15.9
0.3	1.61	0.428	16.9